BRNO UNIVERSITY OF TECHNOLOGY
VYSOKÉ UČENÍ TECHNICKÉ V BRNĚ

FACULTY OF MECHANICAL ENGINEERING
FAKULTA STROJNÍHO INŽENÝRSTVÍ

ENERGY INSTITUTE
ENERGETICKÝ ÚSTAV

CAVITATION EROSION MECHANISMS

MECHANISMY KAVITAČNÍ EROZE

BACHELOR'S THESIS
BAKALÁŘSKÁ PRÁCE

AUTHOR
AUTOR PRÁCE
Helena Kotoulová

SUPERVISOR
VEDOUCÍ PRÁCE
doc. Ing. Pavel Rudolf, Ph.D.

BRNO 2019

VYSOKÉ UČENÍ TECHNICKÉ V BRNĚ
FAKULTA STROJNÍHO INŽENÝRSTVÍ

Zadání bakalářské práce

Ústav:	Energetický ústav
Studentka:	**Helena Kotoulová**
Studijní program:	Strojírenství
Studijní obor:	Základy strojního inženýrství
Vedoucí práce:	**doc. Ing. Pavel Rudolf, Ph.D.**
Akademický rok:	2018/19

Ředitel ústavu Vám v souladu se zákonem č.111/1998 o vysokých školách a se Studijním a zkušebním řádem VUT v Brně určuje následující téma bakalářské práce:

Mechanismy kavitační eroze

Stručná charakteristika problematiky úkolu:

Kavitační eroze je nebezpečný jev vznikající nejen při provozu hydraulických strojů, který může významně ovlivnit jejich parametry (např. účinnost), ale eventuálně i strukturální pevnost. Sledování stupně kavitace na makro úrovni je popsáno v normách pro testování hydraulických strojů., bohužel stále chybí hlubší popis mechanismů vzniku kavitační eroze.

Cíle bakalářské práce:

Cílem bakalářské práce je provedení rešerše mechanismů kavitační eroze (vlivy tlakové vlny při kolapsu kavitační bubliny, microjetu, hot spots, atd.), korelace mezi typy kavitace a agresivitou opotřebení (např. izolované bubliny vs. kavitační mrak) a dalšími faktory, které mohou mít na kavitační opotřebení vliv (např. rychlost vodního proudu, vodivost kapaliny, povrchové napětí, teplota atd.).
Dále bude proveden experiment na kavitační trati odboru s erozí způsobenou hydrodynamickou kavitací a vyhodnocen průběh kavitační eroze.

Seznam doporučené literatury:

KIM, K.H., G. CHAHINE, J.P. FRANC a A. Karimi, ed. Advanced Experimental and Numerical Techniques for Cavitation Erosion Prediction. Springer Netherlands, 2014. ISBN 978-94-017-8538-9.

FRANC, Jean-Pierre a Jean-Marie MICHEL. Fundamentals of Cavitation. Springer, 2006. ISBN 978--4020-2233-3.

BRENNEN, C.E. Cavitation and Bubble Dynamics. New York: Oxford University Press, 1995. ISBN 0195094093.

Termín odevzdání bakalářské práce je stanoven časovým plánem akademického roku 2018/19

V Brně, dne

L. S.

doc. Ing. Jiří Pospíšil, Ph.D. ředitel ústavu	doc. Ing. Jaroslav Katolický, Ph.D. děkan fakulty

ABSTRACT
This bachelor's thesis deals with mechanisms of cavitation erosion and it is divided into two main parts.

The theoretical part describes the principle of cavitation, its inception and mainly the collapse of the cavitation bubbles, which negatively affects the surface of circumflowed solid materials (e.g. at hydraulic machines). For this reason, it is necessary to gain thorough knowledge of the effects of the cavitation erosion.

The experimental part is devoted to cavitation erosion testing of 3D printed metal and plastic samples. The plastic samples were compared with each other and the 3D printed metal samples with the cast ones. The influence of cavitation erosion on 3D manufactured samples is still rather unknown, although it is a very progressive type of manufacturing.

Key words
Cavitation, cavitation erosion, mechanisms of cavitation erosion, 3D printed samples, SLM, FDM

ABSTRAKT
Předložená bakalářská práce se zabývá mechanismy kavitační eroze a je rozdělena na dvě hlavní části.

Teoretická část popisuje princip kavitace, způsob jejího vzniku a především kolaps kavitačních bublin, který negativně ovlivňuje povrch obtékaného tělesa (např. na hydraulických strojích). Z tohoto důvodu je nutné podrobně studovat účinky kavitační eroze.

Experimentální část je věnována testování kavitační eroze na kovových a plastových vzorcích vytisknutých na 3D tiskárně. Plastové vzorky byly srovnávány navzájem mezi sebou, kovové vzorky z 3D tiskárny se vzorky odlitými. O vlivu kavitační eroze na součásti vytisknuté na 3D tiskárně je stále ještě málo informací, i když se jedná o velmi progresivní a stále častěji používaný typ výroby.

Klíčová slova
Kavitace, kavitační eroze, mechanismy kavitační eroze, 3D tisk, SLM, FDM

ROZŠÍŘENÝ ABSTRAKT

Bakalářská práce se zaměřuje na základní principy kavitace, kavitační erozi a její mechanismy. Ke kavitaci dochází v důsledku lokálního poklesu tlaku v mnoha hydraulických strojích. Během kolapsu kavitačních bublin vznikají silné tlakové vlny, jejichž amplituda často překračuje mez kluzu. Proces kolabování bublin je navíc cyklický a vzniká tak únavové namáhání. Zrna materiálu jsou vytrhávána ze struktury a časem dochází k výrazné erozi, která snižuje výkonnost strojů, jejichž díly musí být po určité době vyměněny. Z tohoto důvodu je snaha omezit vznik kavitace – jednak samotnou konstrukcí stroje, jednak použitým materiálem. V současné době se do popředí dostává i druh výroby, jelikož existují různé nové výrobní metody. Jednou z těchto metod, která je stále více využívána a vyvíjena, je 3D tisk.

Práce obsahuje podrobnou rešerši, ze které mimo jiné vyplynulo, že vliv kavitační eroze na vzorky připravené na 3D tiskárně, není skoro vůbec prozkoumán. Doposud se této tématice věnovala jen malá část vědecké komunity, nicméně výsledky jsou velmi slibné - ve srovnání s 3D vytištěným vzorkem a odlitkem, 3D vytištěný vzorek vykazoval nižší hmotnostní ztráty během kavitačního testování. Pravděpodobně neexistuje žádná studie týkající se vlivu kavitační eroze na polymerní materiály. Cílem bakalářské práce tedy bylo tuto problematiku studovat a porovnat odolnost plastových a kovových vzorků zhotovených metodou 3D tisku. Z plastových materiálů byly vybrány materiály Antero 800NA, ABS, ULTEM 9085, Nylon 12 a PolyJet VeroClear a z kovových materiálů hliníková slitina AlSi10Mg a nerezová ocel 316L. Kovové vzorky byly připravovány metodou SLM a jejich kavitační odolnost byla porovnávána s odlitými vzorky, aby mohl být učiněn závěr o vhodnosti jednotlivých metod výroby.

Byly provedeny dva druhy zkoušek - kavitační zkouška v okruhu se clonou a zkouška kavitační eroze kavitujícím paprskem. Pro každou zkoušku bylo vyhodnoceno kavitační číslo pro vyhodnocení kavitační intenzity.

V prvním zmíněném testu byly testovány pouze plastové vzorky a to ve tvaru trubiček. Nebyla však pozorována žádná významná eroze, i když test trval 16 hodin. To může být způsobeno poměrně vysokou hodnotou kavitačního čísla (což znamená nižší intenzitu kavitace). Jediná lehce patrná kavitační eroze byla pozorována u materiálu PolyJet VeroClear, což mohlo být způsobeno nejen materiálovými charakteristikami, ale také orientací jednotlivých vláken, které byly v tomto případě orientovány axiálně vzhledem k tvaru vzorku. Ostatní vzorky byly vytištěny s vlákny orientovanými v obvodovém směru.

Ve zkoušce kavitační eroze kavitujícím paprskem byla pozorována podstatně výraznější poškození povrchu vzorků. Vzorky byly pro tento test vyrobeny ve tvaru kvádrů.

U plastů byla zjištěna závislost kavitační eroze na tlakových materiálových charakteristikách. Materiál Antero 800NA s nejvyšší mezí kluzu v tlaku (a s nejvyšším modulem pružnosti v tlaku) vykazoval nejnižší kavitační erozi. Výsledek tohoto pozorování je vhodné respektovat při výrobě plastových armatur v hydraulických okruzích nebo malých plastových čerpadel. Materiál PolyJet VeroClear opět vykázal nejhorší odolnost vůči kavitační erozi.

Kovové vzorky byly vyrobeny metodou SLM, která vytváří póry ve struktuře materiálu. Konečná struktura však vykazuje dobré materiálové charakteristiky.

V případě nerezové oceli 316L je velmi obtížné rozhodnout, která metoda výroby je lepší, protože počáteční drsnost vzorků byla výrazně odlišná. Lze však konstatovat, že vzorky připravené metodou SLM ukázaly menší procentuální změnu drsnosti a povrch se po experimentu zdál být hladší. Je pravděpodobné, že v průběhu experimentu byly uvolněny neroztavené částice kovového prášku. Navíc mohla na povrchu vzorku vzniknout tenká vrstva oxidů.

Vzorek AlSi10Mg z 3D tiskárny vykazoval lepší odolnost vůči kavitační erozi než odlitek, což je pravděpodobně způsobeno speciální strukturou vzniklou při SLM metodě, zlepšující vlastnosti materiálu. Tento výsledek naznačuje, že je potřeba uvažovat o výrobě komponentů z tohoto materiálu metodou SLM.

V případě plastových materiálů je nutné další zkoumání k určení vlivu orientace vláken. Pokud jde o vzorky z nerezové oceli 316L, je třeba provést více testů, aby mohl být učiněn závěr, který způsob výroby je vhodnější s ohledem na odolnost proti kavitační erozi. Podobná (stejná) počáteční drsnost odlitku a kovového vzorku z 3D tisku je nezbytná pro toto posouzení. V případě slitiny hliníku AlSi10Mg je třeba provést další zkoušky, aby se zjistil vliv tepelných a dokončovacích úprav na vzorky vyrobené SLM metodou. V neposlední řadě je třeba také vyzkoumat vliv různých laserových rychlostí metody SLM.

BIBLIOGRAPHIC CITATION

KOTOULOVÁ, Helena. *Cavitation erosion mechanisms*. Brno, 2019 [cit. 2019-05-22]. Available also at: https://www.vutbr.cz/studenti/zav-prace/detail/117998. Bachelor's thesis. Brno University of Technology, Faculty of Mechanical Engineering, Energy Institute. Supervisor Pavel Rudolf.

DECLARATION

I declare that I have personally compiled the thesis "**Cavitation erosion mechanisms**" according to the instruction of my supervisor, doc. Ing. Pavel Rudolf, Ph.D. and with the use of the sources listed in bibliography.

---------- ----------

Datum Helena Kotoulová

ACKNOWLEDGMENT

I would like to sincerely express my thanks to my bachelor's thesis supervisor doc. Ing. Pavel Rudolf, Ph.D. for his patience, valuable guidance, advice and his willingness to help in every situation. I would also like to thank MCAE Systems for the plastic 3D printed samples; to doc. Ing. David Paloušek, Ph.D. (from DREAT BUT) for the metal 3D printed samples; to Ing. Václav Kaňa, Ph.D. for the cast aluminium alloy; to IPM CAS for the cast stainless steel; to Ing. Martin Hudec and Bronislav Kusý for conducting of the experiments, to Ing. Pavel Gejdoš, Ph.D. and Ing. Martin Juliš, Ph.D. from CEITEC for surface topography and profilometry of samples.

Contents

Introduction

This bachelor's thesis focuses on mechanisms of cavitation erosion. Cavitation occurs as a result of a local pressure drop in many hydraulic machines. During the collapse of cavitation bubbles strong pressure waves are generated, whose amplitude often exceeds the yield stress. Moreover, the process is cyclic and therefore fatigue straining arises. The grains of material are being torn away and over the time a significant erosion occurs, which reduces the performance of machines. Consequently, damaged parts have to be changed after some period of time. For this reason, many steps are taken to reduce a potential of cavitation inception – firstly the adjustment of the machine design and secondly the material of machines. Nowadays, also a type of manufacturing comes to the forefront, as there are various new methods of production. One of these methods, which is more and more used and developed, is a 3D printing.

The aim of this thesis is to investigate the influence of cavitation erosion on 3D printed plastic and metal samples. A very few scientific teams have looked into this problem so far, but their results are quite promising – in comparison of a 3D printed sample and a cast one, the 3D printed sample showed a lower mass loss during the cavitation testing. There is probably no study concerning the effect of cavitation erosion on polymer materials yet. In this thesis, five types of plastic materials (ABS, ULTEM 9085, Nylon 12, Antero 800NA, PolyJet VeroClear) and two metal samples (stainless steel 316L and aluminium alloy AlSi10Mg) are examined. The 3D printed metal samples are also compared with the cast ones.

1 Cavitation

1.1 Principle of cavitation

Cavitation is a physical phenomenon describing the formation of cavities in a liquid due to a local pressure drop. These cavities are filled with vapors of ambient liquid and gases. There are two ways to achieve a liquid-to-gas transition – either by lowering the pressure at steady temperature and subsequent cavitation, or by raising the temperature of the liquid under constant pressure and consequent boiling. Cavitation becomes very dangerous especially when a fluid flows around solid materials. The collapse of a cavity is accompanied by increased pressure, temperature and shock waves that adversely affect the surface of the nearby material. Significant erosion occurs over the time which causes that a component has to be excluded from operation. Cavitation, however, may not always be just a negative matter, it can be used e.g. for the removal of micro-organisms in the water [1], [2], [3], [4].

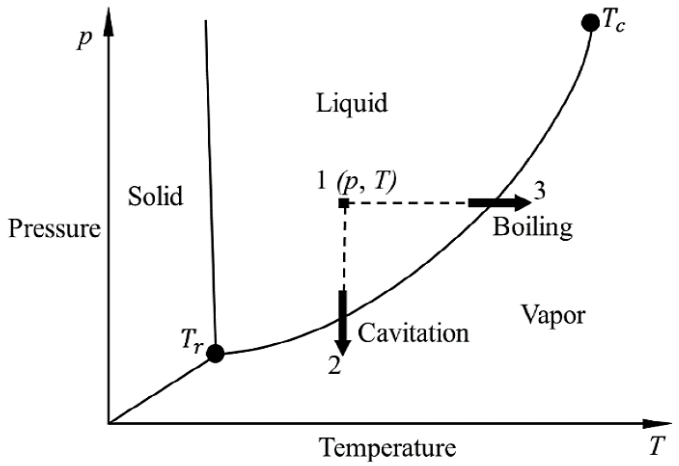

Fig. 1: Phase diagram showing the transition of liquid into gas [5]

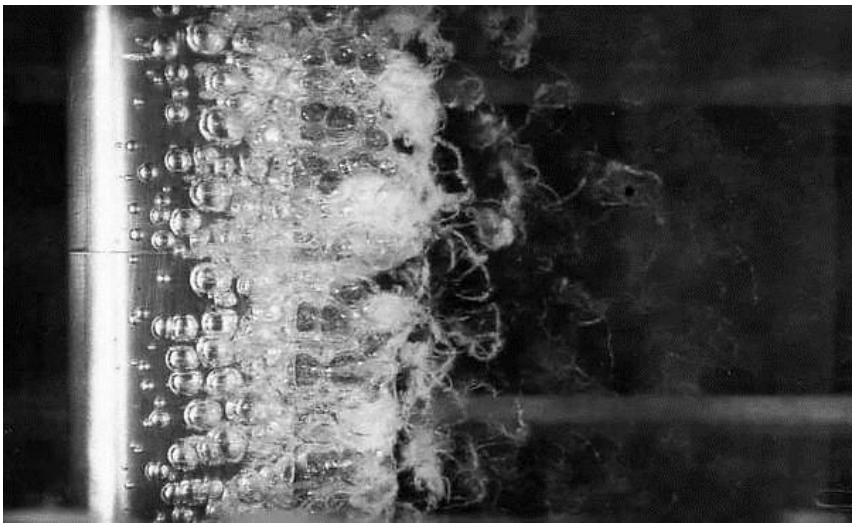

Fig. 2: The formation of cavitation bubbles on the ship's screw propeller [6]

1.2 Types of cavitation

Cavitation can be differentiated according to the way of its formation. It can be induced either by laser (laser cavitation), or ultrasonic waves (acoustic cavitation) or due to a local pressure drop (hydrodynamic cavitation).

The creation of *laser cavitation* lies in a rapid increase of energy at a particular point of the fluid due to the presence of a strong source of electromagnetic radiation, resulting in a significant local heating of the liquid. Consequently, hot plasma (6000-15 000 K) occurs at this spot. As a result of high temperatures, liquid evaporates and cavities are formed [7].

Acoustic cavitation is formed by ultrasonic waves in a liquid. High frequencies lead to an inception of pressure waves that make a liquid oscillate. The magnitude of bubbles changes according to the amplitude of waves [1].

Hydrodynamic cavitation is a result of a rapid pressure drop within various hydraulic machines - pumps, turbines, valves, propellers, and so on [1]. Chapter 2 is devoted to this problem in detail.

1.3 Technological use of cavitation

Cavitation generally has a rather negative effect (in particular, erosion of materials in case of hydrodynamic cavitation), but there are also technological areas that benefit from cavitation.

Acoustic cavitation is extensively used for a cleaning of small or shape-demanding items (e.g. jewellery), as well as for a removal of scales and other impurities in the steel industry, or for creating various emulsions and solutions. In medicine, for a removal of tartar and kidney stones by a non-operative way (lithotripsy) [8].

During the collapse of acoustically induced cavitation an interesting phenomenon of sonoluminescence is observed. This phenomenon is probably caused by an intensive compression of a gas in a bubble, which causes the gas to become hot (creation of hot spots, see Chapter 3.1.4) and also by the emission of electromagnetic radiation [1]. The same conditions are applied in sonochemistry. Sonochemical decomposition of substances is of great importance in the preparation of samples of metals, alloys, carbides, etc. with nanostructure and in the production of biomaterials. A very important group of biomaterials makes up protein microspheres, which are very useful in medicine, for example for drugs transfer, or highlighting contrasts in magnetic resonance, etc. [10].

Both acoustic and hydrodynamic cavitation are also significant in the field of water purification and disinfection, where a high pressure generated by the collapse of cavitation bubbles is used. There are also various chemical processes (in case of acoustic cavitation - sonochemistry, in case of hydrodynamic cavitation - hydrodynamically induced chemistry), which help to remove bacteria and impurities in water [3], [4].

2 Hydrodynamic cavitation

Hydrodynamic cavitation is a process of formation of cavities (bubbles) in a liquid when the pressure drops to a saturated vapor pressure value. Consequently, liquid continuity is disrupted and first cavitation bubbles are formed. Cavities can move in a flowing fluid, and once they get to a place with a higher pressure, they collapse violently (implode). As mentioned above, hydrodynamic cavitation has adverse effects on hydraulic machines, whose performance is thereby reduced [1].

2.1 Types of hydrodynamic cavitation [1]

Hydrodynamic cavitation takes many forms, which depend on hydrodynamic conditions (velocity of a flow, pressure of a liquid, etc.), properties of the liquid and a geometry of a circumflowed profile.

Hydrodynamic cavitation can be divided e.g. according to its motion:

- *Transposing one* – cavities are formed and collapse during a motion in the flow direction
- *Non-transposing one* – a cavitation region is connected to a circumflowed body
- *Supercavitation* – a cavitation zone closes behind a circumflowed body

In case of *pseudo-cavitation* there is a bubble with a large initial radius filled with a great amount of air. The radius of a bubble increases at a pressure higher than the saturated vapor pressure of a liquid, and therefore there is no diffusion of gases into the bubble. Its collapse is not so dramatic, and does not lead to significant damage of materials. Its occurrence can distort results of cavitation tests.

Another significant type of cavitation is a *vortex cavitation* (see Chap. 3.1.7), which occurs in the core of a vortex where the pressure is considerably lower than in surrounding liquid.

A special group includes *clouds of bubbles* (see Chap. 3.1.5) whose collapse is very aggressive and leads to serious damage.

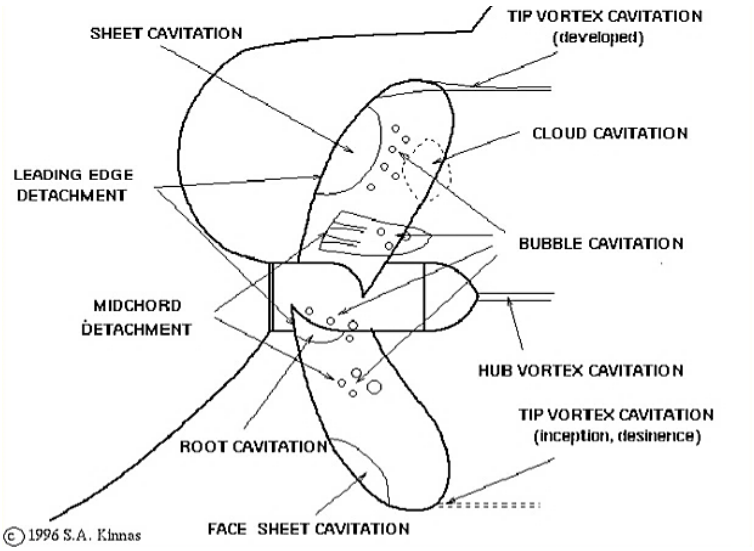

Fig. 3: Types of hydrodynamic cavitation shown on the propeller blades [11]

2.2 Mathematical tools for description of hydrodynamic cavitation

2.2.1 Rayleigh-Plesset equation

Rayleigh-Plesset equation is one of the most important equations in the field of hydrodynamic cavitation. It is a differential equation describing dynamic behaviour of spherical bubbles filled with vapor or gas in an infinitely large and incompressible liquid [6].

In general, this equation is as follows:

$$\frac{p_B(t)-p_\infty(t)}{\rho}=R\ddot{R}+\frac{3}{2}(\dot{R})^2+\frac{4\nu_L}{R}\dot{R}+\frac{2\sigma_L}{\rho R}, \tag{2.1}$$

where $R(t)$ is a bubble radius, ρ is the density of the surrounding liquid, v_L is the kinematic viscosity of the liquid, σ_L is the surface tension at an liquid/bubble interface, $p_B(t)$ is a homogenous (uniform) pressure in the bubble and $p_\infty(t)$ is a pressure at an infinite distance from the bubble [6].

It is based on the law of mass conservation (or continuity equation) - a growth of a bubble size must be equal to an amount of a liquid entering it. In addition, the law of momentum conservation is also applied on the assumption that a fluid surrounding a bubble has properties of a Newtonian liquid[1]. In such cases, the Navier-Stokes[2] equation for motion in radial direction can be used for a description of a Newtonian incompressible fluid flow [6].

2.2.2 Cavitation number

The cavitation number describes how significant the cavitation phenomenon is. It is a relationship between pressure and velocity [2]:

$$\sigma=\frac{p_\infty-p_v}{\frac{1}{2}\rho v_\infty^2}, \tag{2.2}$$

where p_∞ is a reference pressure, p_v is the saturated vapor pressure, ρ is the density of a liquid and v_∞ is a reference velocity [2]. It is evident that the cavitation number increases with decreasing reference velocity and/or with increasing reference pressure. At high σ, cavitation does not occur and vice versa with decreasing σ, cavitation is more developed [2].

---

[1] Newtonian fluid is a substance that satisfies Newton's law of viscosity: $\tau=\mu\frac{du}{dx}$, which is a relation describing the direct proportion between stress τ and deformation velocity du/dx; the constant of proportionality is dynamic viscosity μ [12].

[2] This equation can be written in spherical coordinates like: $-\frac{1}{\rho}\frac{\partial p}{\partial r}=\frac{\partial u}{\partial t}+u\frac{\partial u}{\partial r}-\nu_L\left[\frac{1}{r^2}\frac{\partial}{\partial r}\left(r^2\frac{\partial u}{\partial r}\right)-\frac{2u}{r^2}\right]$, where r is a coordinate, expressing a distance from the centre of a bubble, $u(r,t)$ is an outward velocity, $p(r,\ t)$ is pressure, ρ is density of a liquid, ν_L is kinematic viscosity of a fluid [6].

The critical value of the cavitation number at which first cavitation bubbles are incepted can be defined as [6]:

$$\sigma_i = -C_{p\min}, \tag{2.3}$$

where C_{pmin} is a minimum of a pressure coefficient C_p [6]. The pressure coefficient

$$C_p(x_i) = \frac{p(x_i) - p_\infty}{\frac{1}{2}\rho v_\infty^2} \tag{2.4}$$

describes relative pressure throughout a flow of an incompressible liquid with constant density ρ, velocity field $v_i(x_i)$ and pressure $p(x_i)$ [6]. Again, p_∞ is the reference pressure and v_∞ is the reference velocity. Each point has its own pressure coefficient. It is a dimensionless quantity and usually its values are negative [6].

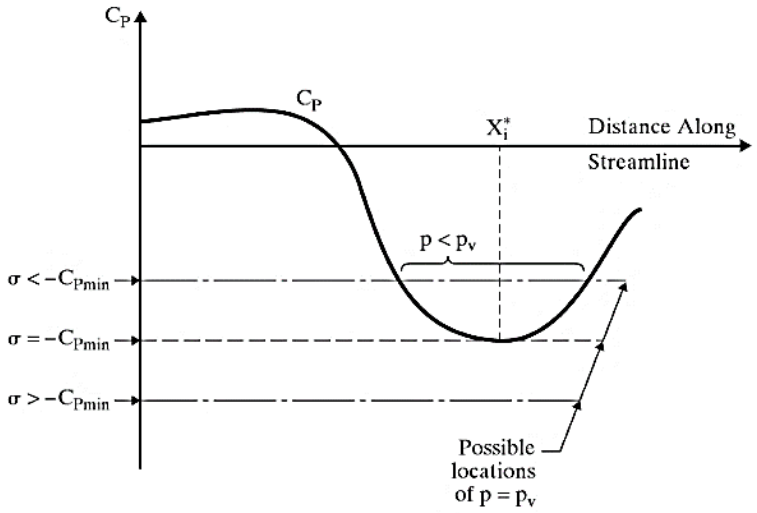

Fig. 4: A scheme of pressure distribution on a streamline; $C_p(x_i^*) = C_{pmin}$ [6]

There are three possible situations as it can be seen in Fig. 4. For $\sigma > -C_{pmin}$ pressure is greater than p_v, so that cavitation does not occur. When $\sigma = -C_{pmin}$, pressure p reaches the value of p_v and first cavitation bubbles are formed. For $\sigma < -C_{pmin}$ cavitation becomes more developed [6].

The cavitation number can also be used as a comparison parameter or similarity number when dealing with liquid flowing around various bodies, such as spheres, cylinders, profiles of channels, etc. [1].

2.3 Creation of hydrodynamic cavitation

Cavitation bubbles arise in places where fluid cohesion has been disrupted. When the cohesive (attractive) forces in a fluid are overcome, a small crack that disrupt the continuum is created and can become a source of cavitation. In addition, real liquids are not perfectly clean but contain various impurities, mechanical particles or bubbles of undissolved gas. It is assumed that these bubbles of undissolved gas, which act as cavitation nuclei, have the greatest impact on the creation of a cavitation. They appear in microscopic cracks of a body surface subjected to the flow and also adhere to small particles that are contained in the liquid. Cavitation bubbles are also filled with saturated vapors of the surrounding liquid. When a pressure drops to the saturated vapor pressure and a critical radius is exceeded, cavitation bubbles are formed from cavitation nuclei. If the pressure remains the same, or even reduces, the cavity radius grows. However, if cavitation bubbles move to a higher pressure area, they collapse dynamically [1], [8].

Cavitation arises for example in narrowed points of a pipeline or in channels as a result of a local pressure drop. By reducing the cross-sectional area, the fluid velocity will increase (the continuity equation[3]) and thus the pressure will reduce (the Bernoulli equation[4]). When a pressure drops to the saturated vapor pressure, it leads to the phase transformation (liquid to vapor) and cavitation occurs [1].

A formation of cavities due to vortices is called a vortex cavitation, closely related to hydrodynamic cavitation. Vortex[5] can arise during circumfluence of various profiles, bodies, or surface waviness (unevenness), but also e.g. behind a screw-propeller [1].

To create a vortex cavitation, this condition must be valid [1]:

$$p_{cav} > p_{\varphi} = p_k - \rho \frac{v_{\varphi}^2}{2}, \tag{2.5}$$

where p_k is a pressure of a surrounding liquid. Velocity of the vortex in its core v_{φ} at the radius r_{φ} can be expressed as [1]:

$$v_{\varphi} = \frac{rv}{r_{\varphi}}, \tag{2.6}$$

where v is the velocity of the vortex at its edge – at radius r. Velocity v_{φ} is also the circumferential (tangential) velocity of the potential vortex (vortex with zero turbulence, $\omega = 0$), where individual particles of a fluid do not rotate themselves, they just simply move on a circular trajectory. The value of this velocity decreases with increasing distance from the center of rotation. Potential vortices serve only to simplify the problem (under certain conditions - especially the high Reynolds number), but cannot actually occur [9].

[3] $S \cdot v = const.$ [13]

[4] $\frac{v^2}{2} + \frac{p}{\rho} - U = B_{const.}$ [13]

[5] Whether a flow is laminar or turbulent (vortex) depends on Reynolds number: $Re = \frac{v \cdot D_H}{\nu}$ [-]. The critical value of Reynolds number for pipes is around 2320. For *Re* >> 2320 the flow is turbulent [13].

2.4 Physical properties of fluid influencing cavitation

Influence of surface tension of liquid

Surface tension is related to fluid cohesion. The higher the surface tension of a liquid is, the lower pressure there is needed for cavitation, and the growth of a bubble is slowed down. Higher surface tension therefore has anti-cavitation effects. Simultaneously, however, the cavitation disappears more rapidly as a liquid tries to return to a cohesive state [1], see Fig. 5 below.

Influence of fluid viscosity

Viscosity represents internal frictional forces of a fluid. When the viscosity of a fluid increases, its velocity decreases and its pressure increases, thus the conditions for the cavitation inception worsen. Experiments, however, have come up with opposite conclusions in some cases [1].

The significance of frictional forces in a fluid is also related to the dissipation of mechanical energy, which leads to absorption of oscillation of cavitation bubbles. Therefore, in a fluid with greater viscosity, the radius of a cavitation bubble will grow (or contract) more slowly in comparison to less viscous fluid [8].

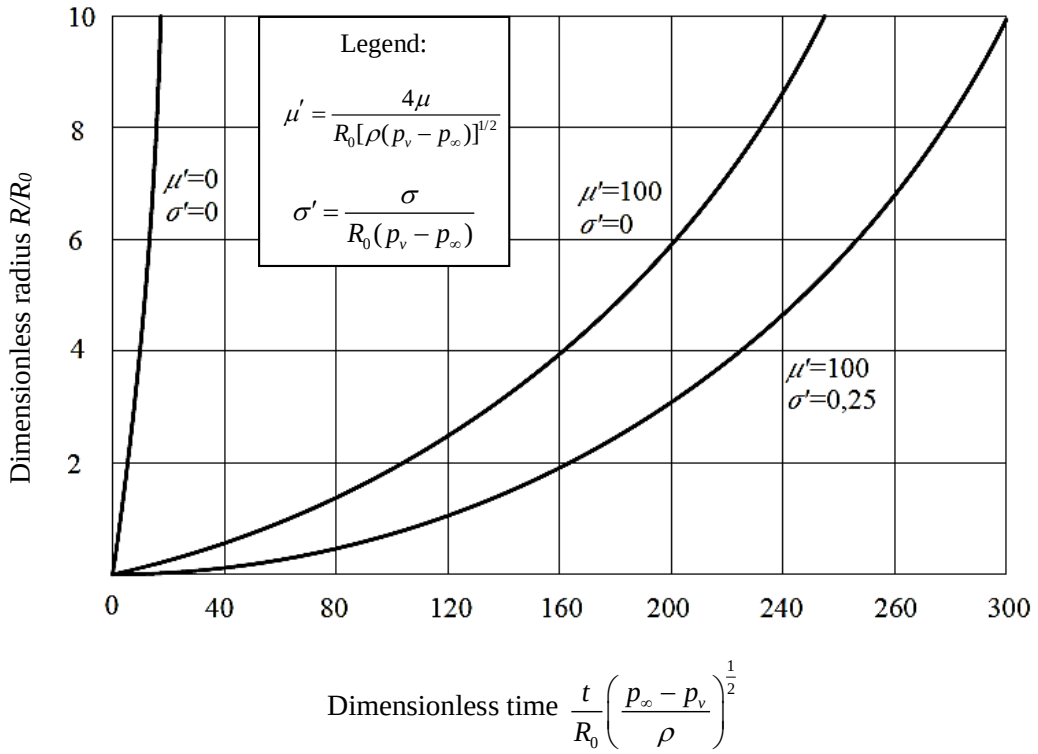

Fig. 5: Influence of dimensionless viscosity μ' and dimensionless surface tension σ' on the growth of the radius of the cavitation bubble in an incompressible fluid, adapted from [8].

Influence of compressibility of fluid

Liquid compressibility is a significant physical property of real fluids, affecting in particular the process of a cavitation bubble collapse. During the cavity collapse fluid velocity of a compressible liquid can be up to one order less than in case of an incompressible liquid. However, with minor changes in pressure, this effect is negligible and is usually considered only when a cavity collapses [8].

Equations describing hydrodynamic cavitation (such as the Rayleigh-Plesset equation) did not originally take the influence of compressibility into account and were formulated for incompressible liquids. But later, modifications of equations (Gilmore, Keller-Miksis) including this influence [8] were created.

Influence of air content

The more the bubble is initially filled with air, and the larger the initial radius is, the greater the cavitation pressure there is needed. In case of larger cavitation cores, it is therefore easier to achieve cavitation [1], as it is also evident from Fig. 6.

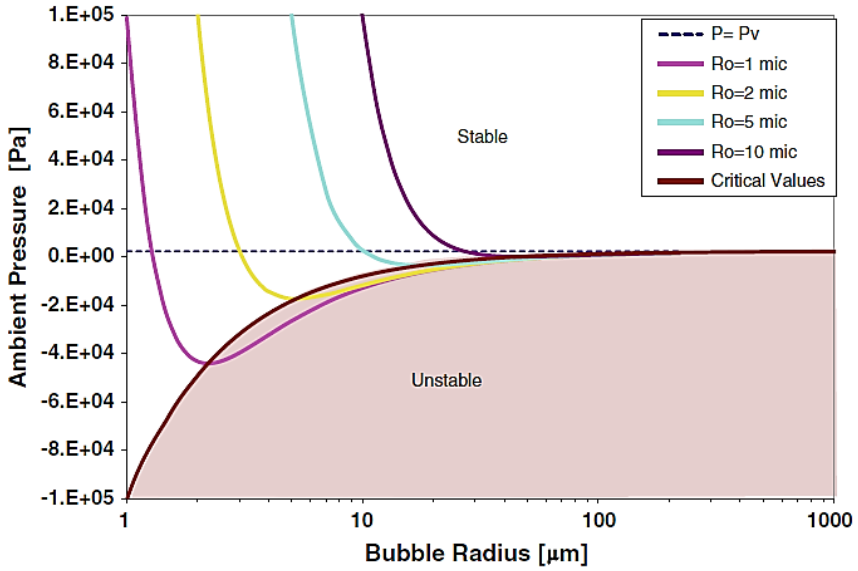

Fig. 6: Curves of static equilibrium for spherical bubbles with various initial radii [2]

The dashed curve joins minima of individual curves which illustrate the course of fluid pressure for particular initial radii of bubbles. Individual minima are denoted R_K - critical radii. When a pressure drops below the saturated vapor pressure and critical radius is reached, the radius of a bubble starts to grow explosively [8].

Influence of fluid temperature

There are more opinions on the influence of temperature, so that different views can be found in different sources. According to the experimental results, an increasing temperature increases the anti-cavitation effect, which can be explained through the phase diagram and thermodynamic processes. Increasing temperature increases the pressure of a liquid, but the cavitation needs a rather low pressure to originate [1]. On the other hand, an increase of temperature at constant ambient pressure supports cavitation [14].

3 Cavitation collapse and erosion

3.1 Mechanisms of cavitation collapse and erosion

There are a lot of hypotheses describing the collapse of a cavitation bubble, among the most well-known are the micro jet theory, hot spots, the inception of pressure waves at collapse, etc.

3.1.1 Collapse of a single cavitation bubble

The cavity collapse is a very fast process that is difficult to be observed. However, it was found out that when a bubble returns to higher pressure locations, it first stops growing (at its maximum radius R_M, which is approximately 100 times bigger than an initial nucleus radius R_0) and then implodes. The bubble pressure is relatively low at the bubble's maximum volume and is close to the saturated vapor pressure, while the pressure of a surrounding liquid is substantially higher. As a consequence, the collapse of the cavitation bubble is a very dynamic and aggressive process.

During the implosion a bubble is being compressed. Eventually, the bubble cannot be compressed more, because of the volume of vapors the bubble contains. Consequently, the bubble contents spring back and the bubble rebounds a few times (see Fig. 7).

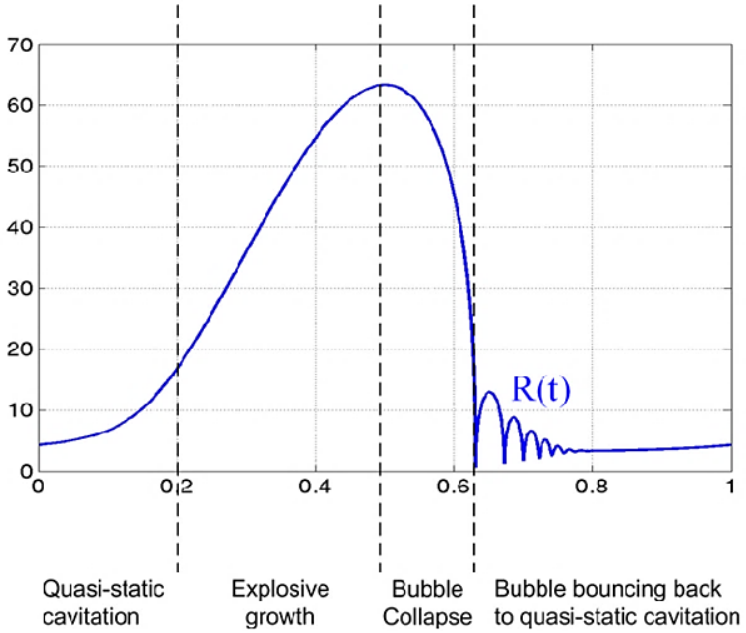

Fig. 7: Bubble rebounding [15]

3.1.2 Micro jet

Micro jet, a narrow liquid beam, occurs during a non-symmetrical collapse of a bubble. There is an unstable interface between a liquid and a shrinking cavity (bubble), which means that even a slight shift from this unstable equilibrium state leads to the formation of a micro jet. A wall subjected to the fluid flow is deformed first – the jet of the liquid gets into the centre of the cavity through a small hole arising in the bubble wall. The bubble also gets a shape of a ring [8].

The situation, when the bubble collapses near a solid surface, is very interesting. The bubble tends to collapse faster on the side remoted from the body wall, which results in the liquid jet being directed focused onto the solid surface of the body. The jet has a very high velocity (approximately the speed of sound in a liquid) and hence energy. There is a significant local increase of temperature and pressure at the impact point of the jet and pressure waves and noise will occur [8].

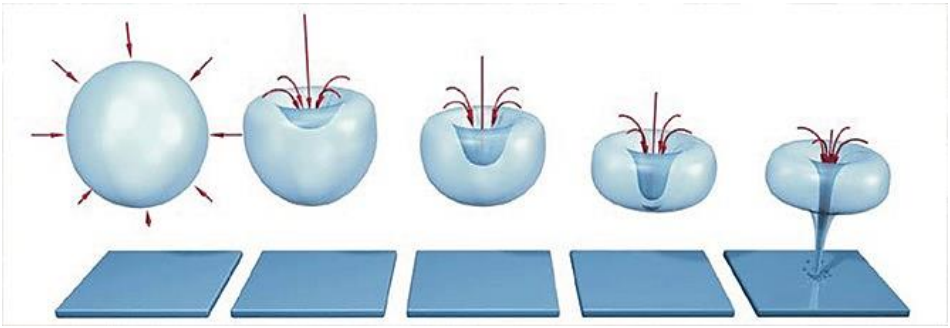

Fig. 8: An annular shape of collapsing bubbles and a micro jet [16]

A pressure developed due to this fast-moving liquid beam is particularly significant. The velocity of the micro jet v_j is in the order of hundreds of m/s and the pressure is described by the Joukowski equation [14]:

$$\Delta p = \rho c v_j, \tag{3.1}$$

where c is the speed of sound. For water we often get value Δp = 150 MPa. However, the duration of the micro jet is very short and ranges in the order of $d/2c$, where d is a diameter of the micro jet. The diameter of the micro jet has a value of about 0.1 mm for 1 mm diameter bubble, and the time the pressure acts on the surface of a component is about 0.03 μs [14].

3.1.3 Divergent spherical pressure waves

Symmetric collapse of a bubble causes compression of cavity content, increase of internal temperature and pressure and consequent inception of divergent spherical pressure waves, which disrupt the surface of the nearby solid body. Despite the fact that it is a very fast process (around 1 μs), the pressure reaches values in the order of hundreds of MPa, which is the same order as for the micro jet. The amplitude of a pressure wave decreases with increasing distance from the centre of the bubble [8].

Spherical pressure waves and micro jet produce great pressure of the same order as the yield strength of most metals. But both phenomena only last for a short while. However, the duration increases with increasing bubble size [14].

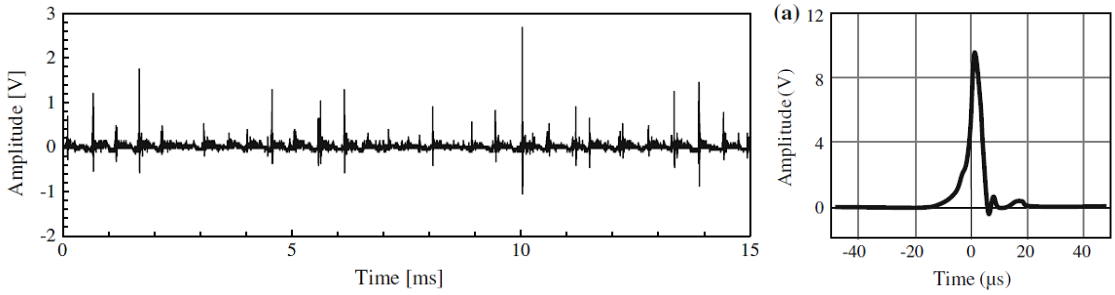

Fig. 9: Pressure course (piezoelectric method) – *left*, detail of a pressure pulse (*right*) [2]

3.1.4 Hot spots

The theory of hot spots states that the collapse of a cavitation bubble proceeds almost adiabatically. Adiabatic compression of gas contained in the bubble causes a significant increase in temperature and pressure. At the same time, a thin layer is formed, covering the hot core. However, this layer has a lower temperature [17].

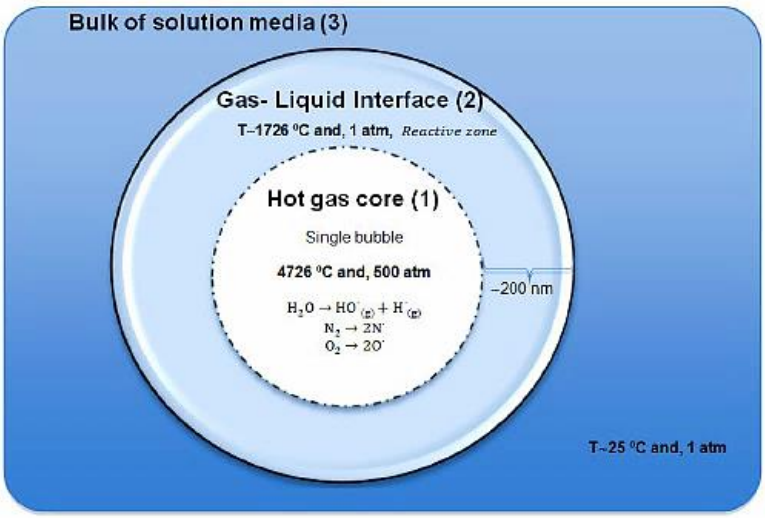

Fig. 10: Model of hot spots [17]

The process of cavity collapse also causes changes in electrical resistance and thermal conductivity of a fluid, and it influences chemical reactions. As it can be seen from Fig. 10, the adiabatic collapse of the cavity results in a decomposition of water to the hydrogen ion H^+ and the free OH^{-1} radical. Subsequently, an oxidation-reduction reaction causes formation of hydrogen peroxide H_2O_2, which is of great importance for destroying microorganisms and bacteria in the field of disinfection and purification of waste water [3].

As mentioned above, acoustic cavitation results in sonoluminescence. In case of hydrodynamic cavitation, it is only luminescence, but the principle of its inception is the same. Due to the strong compression, gas becomes very hot and subsequently it emits electromagnetic waves radiation [1].

3.1.5 Clouds of bubbles

This is an important area of the hydrodynamic cavitation, as the dynamics of bubble cloud movement is very different from the behaviour of individual bubbles.

The cloud cavitation can be formed on a hydrofoil, which is subjected to the fluid flow at changing angles. When the angle of attack increases, cavitation bubbles grow and form a sheet cavitation [18].

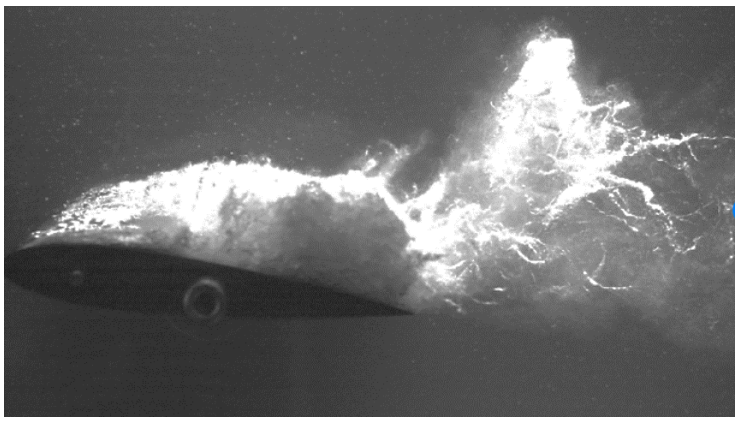

Fig. 11: Cloud cavitation on hydrofoil [36]

The cloud cavitation can be also generated by the vibratory cavitation apparatus (see Chap. 4.1.) [2].

The behaviour of clouds of bubbles can be described by parameter β defined by Luca D'Agostino. He introduced three basic parameters for the spherical cloud bubble - the radius of the cloud A, the average bubble radius R and the coefficient α, which represents the volume fraction of the gas enclosed in the cloud. The parameter β is defined as [37]:

$$\beta = \frac{\alpha_0 A_0^2}{R_0^2}, \tag{3.2}$$

where index 0 represents the initial state [37].

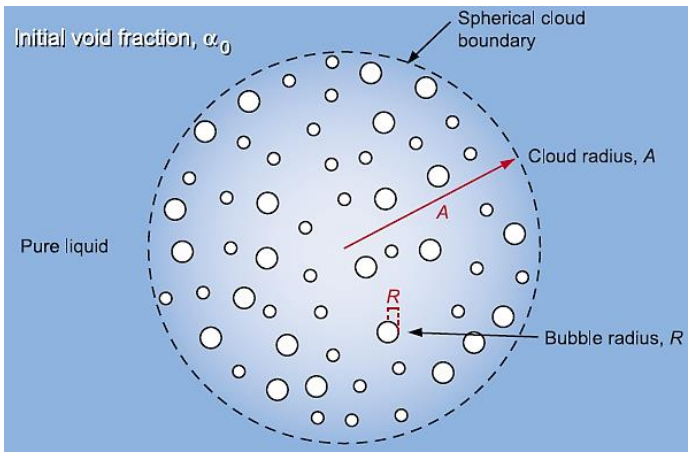

Fig. 12: The cloud of bubbles and its parameters [37]

If β is greater than 1, it means that the cloud is densely filled with bubbles, or has a large radius *A*. In this case, bubbles on the surface of the cloud grow most significantly and then they also collapse first, and the collapse spreads inwards into the bubble. Pressure waves caused by the collapse of the cloud of bubbles with parameter $\beta > 1$ may reach values up to 1 MPa [37].

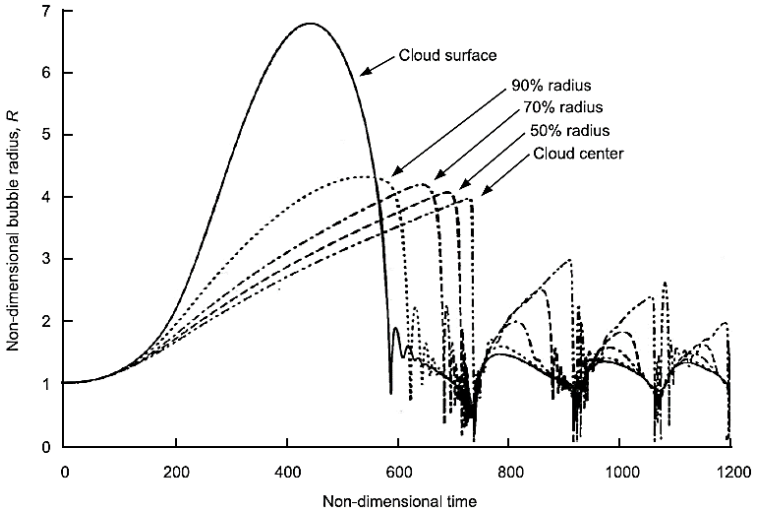

Fig. 13: Growth of the bubble radius in relation to time for $\beta > 1$; bubbles on the surface grow the fastest and the most significantly [37].

If the cloud is not too filled with bubbles and so $\beta < 1$, the bubbles on the surface grow even faster than in the previous case. The collapse of the cloud, however, begins at its centre and spreads to its edge. The resulting wave is considerably weaker than in case of collapse spreading into the cloud and its impact is almost negligible [37].

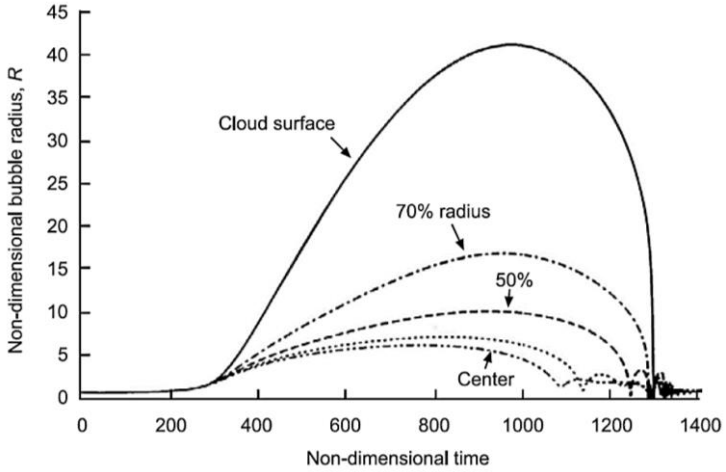

Fig. 14: Growth of bubble radius in relation to time for $\beta < 1$ [37]

The collapse of the bubble cloud can be described as a cascade. The collapse of individual bubbles induces pressure waves that cause collapse of surrounding bubbles, and consequently a significant increase in the amplitude of the pressure wave. The collapse of the cloud of bubbles leads to incomparably greater shockwaves, noise and, of course, to the corresponding damage [14].

3.1.6 Electrochemical effects of cavitation

When a bubble collapses near a solid body surface, a small part of the surface is heated up, creating a thermoelectric couple with the surrounding cool material. This process leads to electrochemical corrosion of the surface layer of the material. Corrosion generally increases a susceptibility to the inception of little cracks and leads to cavitation erosion [8].

3.1.7 Vortex cavitation

Cavitation also arises in vortices created by screw-propellers, impellers or water turbines. The vortices have a significant suction in their centre due to the centrifugal forces of the rotating fluid, which leads to the inception of bubbles [1].

While, for example, the ship's screw-propellers produce surprisingly stable vortices, water turbines create rather unstable and variable vortices [14].

Fig. 15: Vortex cavitation of the screw-propeller [19]

Fig. 16: Vortex cavitation of Francis turbine [6]

Vortex cavitation generates foamy clouds of bubbles and possible cascade collapse. As a consequence, significant cavitation erosion develops, not only because the pressure during the collapse is of the same order as in case of the micro jet or spherical pressure waves but also because the collapse process lasts longer - it can reach up to several tens of microseconds [14].

3.2 Material erosion

The aforementioned effects together negatively affect the quality of a solid body surface. At first these effects lead to roughening of the surface and creation of microscopic craters, afterwards the flow of the liquid washes away the released material. The longer the cavitation lasts, the greater the damage, gradually leading to a significant erosion of material.
In addition, released parts of the material may cause a breakdown of the machine [1].

The collapsing bubble only affects a small part of a surface, comparable to the size of material grains or other structural components. Individual grains of material are being chipped as a result of the gradual process of cavitation collapse, which suggests that with the increasing inhomogeneity of the surface, the intensity of cavitation erosion grows [8].

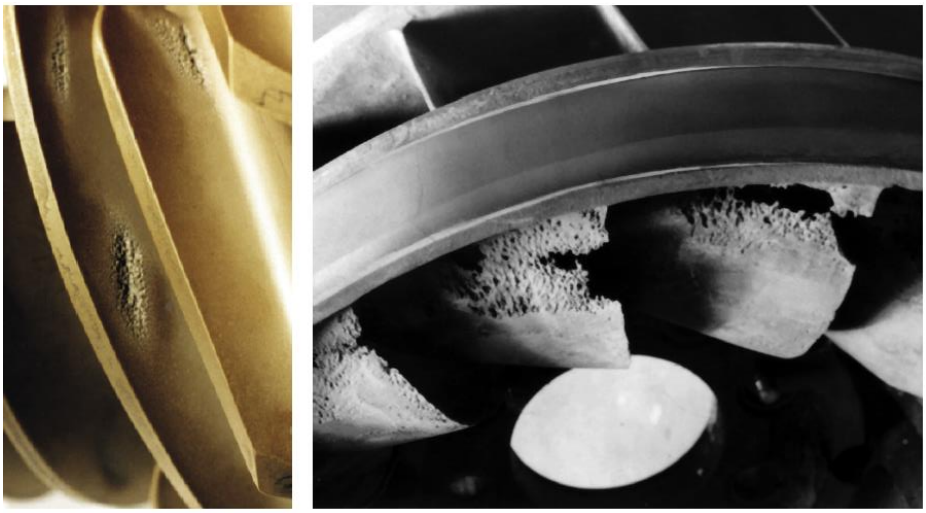

Fig. 17: Early signs of cavitation damage versus damage caused by long-acting cavitation [37]

3.2.1 The influence of material selection and its cavitation resistance

Cavitation erosion concerns perhaps all materials - metal, glass, cement, rubber, or other material. Likewise, the inception of cavitation bubbles does not only concern water but also mercury, liquid lithium, etc. [8].

During the cavitation erosion of a material, tensile stress occurs in a surface layer, which is larger or equal to the yield stress. Thus, for example in soft metals such as nickel and titanium, plastic deformation occurs almost simultaneously with the occurrence of cavitation. On the contrary, in case of hard materials (e.g. tungsten), cavitation erosion occurs with a delay [8].

The effects of water shocks and pressure waves lead to cumulation of material damage and corresponding plastic deformation. Material fatigue occurs and may result in fatigue fracture [8].

If corrosion occurs in a material, it is exposed to a higher risk of cavitation erosion. The corrosion gives rise to slight but very dangerous cracks that are spreading and increasing over time. Most corrosion-resistant materials are also well resistant to cavitation erosion, but there are also exceptions such as gold, glass, etc. [8].

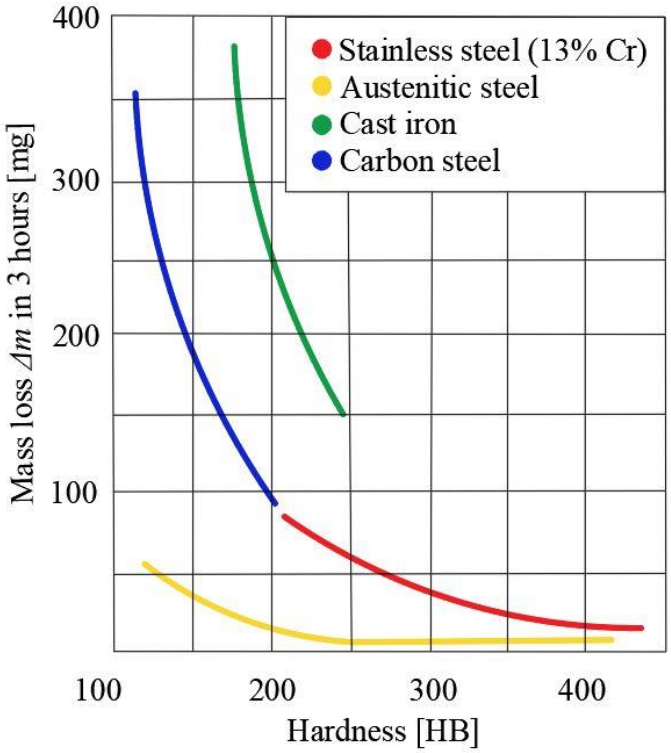

Fig. 18: A comparison of cavitation erosion resistance of various materials, adapted from [20]

3.2.2 Influence of impact waves on material

As mentioned above, micro jet and divergent spherical pressure waves are sources of pressure of high intensity and short duration. These short but strong pressure pulses lead to plastic deformation in the form of lattice defects, dislocations and twinning [2].

The mechanical properties of materials depend on the strain rate, which is defined as [2]:

$$\dot{\varepsilon} = \frac{\Delta\varepsilon}{\Delta t} = \frac{\Delta l}{l}\frac{1}{\Delta t} = \frac{\Delta l}{\Delta t}\frac{1}{l} = \frac{v}{l}, \tag{3.3}$$

where $\Delta\varepsilon$ is a relative elongation caused by shock stress, Δt is a duration of the pressure pulse, l is a linear dimension of the plasticized area, and v is a displacement velocity of the affected part of a surface [2].

It can be seen from Eq. (3.3) that the strain rate is measured in s^{-1} unit. Fig. 19 shows the dependence of flow stress on strain rates for different types of materials. Flow stress is a quantity representing an immediate stress required to maintain plastic deformation in a material, e.g. deformation of value of 0.2 % corresponds to the yield stress according to the tensile curve [2].

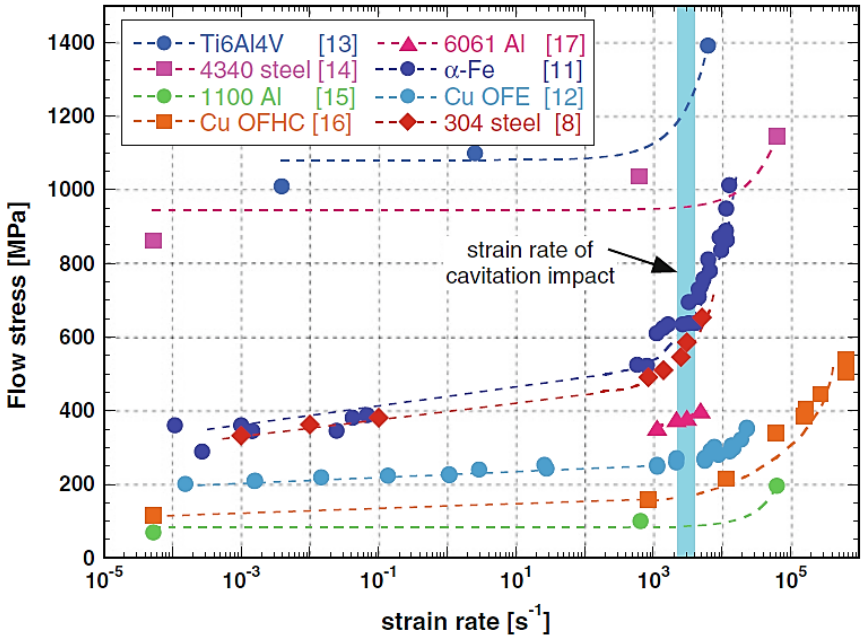

Fig. 19: Dependence of flow stress on strain rate [2]

It can be seen from Fig. 19 that for $\dot{\varepsilon} < 10^3 \mathrm{s}^{-1}$ the strain rate does not have a large effect on the flow stress. However, for $\dot{\varepsilon} > 10^3\ \mathrm{s}^{-1}$there is a significant increase of the flow stress and consequently it leads to the hardening of the material. Shock waves most often cause a deformation ε of about 3 – 5 % but are capable of achieving deformation of values up to 15 – 16 %. On the average they last around 10 μs. For these values, the strain rate can be calculated as [2]:

$$\dot{\varepsilon} = \frac{\Delta\varepsilon}{\Delta t} = \frac{5 \cdot 10^{-2}}{10 \cdot 10^{-6}} = 5 \cdot 10^3 \mathrm{s}^{-1}, \tag{3.4}$$

which is the value that separates the region of low and high deformation rate in Fig. 19.

High strain rates lead to bigger displacements, larger concentration of vacancies in crystal lattices, and more significant tendency to twinning than at low strain rates [2].

3.2.3 Mass and volume loss

Cavitation erosion increases with the increasing velocity of the fluid flow relative to the wall of a vessel. Dependence of mass loss $\dot{m}$ on the flow velocity v can be expressed by the following equation [14]:

$$\dot{m} = k(v - v_0)^n, \tag{3.5}$$

where n ranges from 4 to 9 (most often around 7) and v_0 is the ultimate velocity at which cavitation still occurs. At velocities lower than v_0 there is no cavitation or it is negligible. The higher the exponent n, the greater the damage [14].

Concerning the volume loss, some empirical equations were obtained – e.g. for the aluminium alloy Al 7075 in a cavitating liquid jet test (ASTM G134, see Chap. 4.2) [2]:

$$V^* = 1,2 \cdot 10^{-9} \cdot v_j^{4.43}, \tag{3.6}$$

where V^* [mm^3] is the characteristic erosion volume loss and v_{jet} [m/s] is the velocity of the cavitating liquid jet. It can be seen from Eq. (3.6) that the volume loss grows significantly with the increasing cavitating jet velocity [2].

Volume (respectively mass) loss also varies over time. In the so-called incubation period there is no volume loss, but then follows an acceleration period in which the volume loss significantly increases until it reaches a deceleration period. After a certain amount of time, the cavitation achieves a steady state [14].

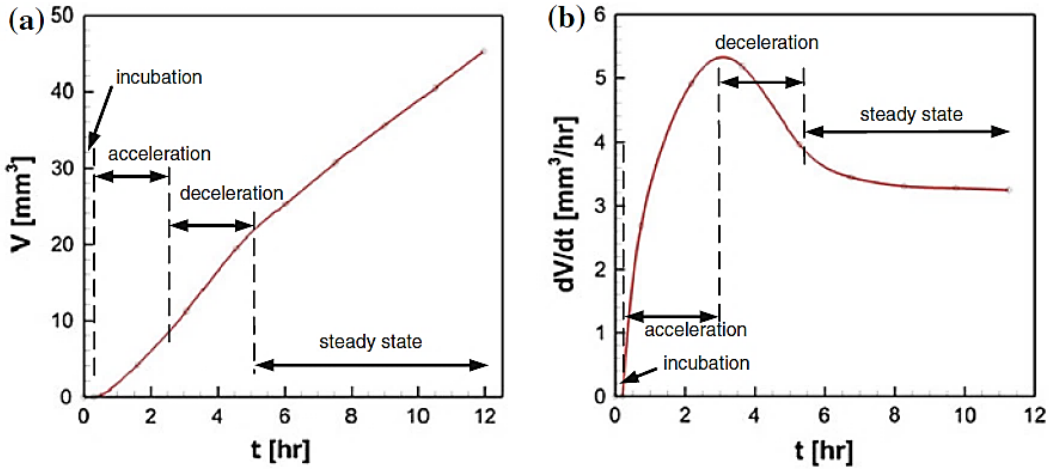

Fig 20: a) The progress of volume loss over time (S-curve, cumulative graph), b) the dependence of rate of volume loss on time [2]

In the *incubation period*, only microscopic pits of approximately circular shape occur on the surface of the material occur. The pits are formed by plastic deformation induced by shock waves and micro-jets. The plastic deformation also leads to work hardening of the surface. The pits are only visible on the polished surface because the surface waviness caused by them can be easily confused with its roughness. In view of that these small pits do not overlap substantially, their number and their other characteristics can be used to calculate the power and aggressiveness of the liquid flow [14], [2].

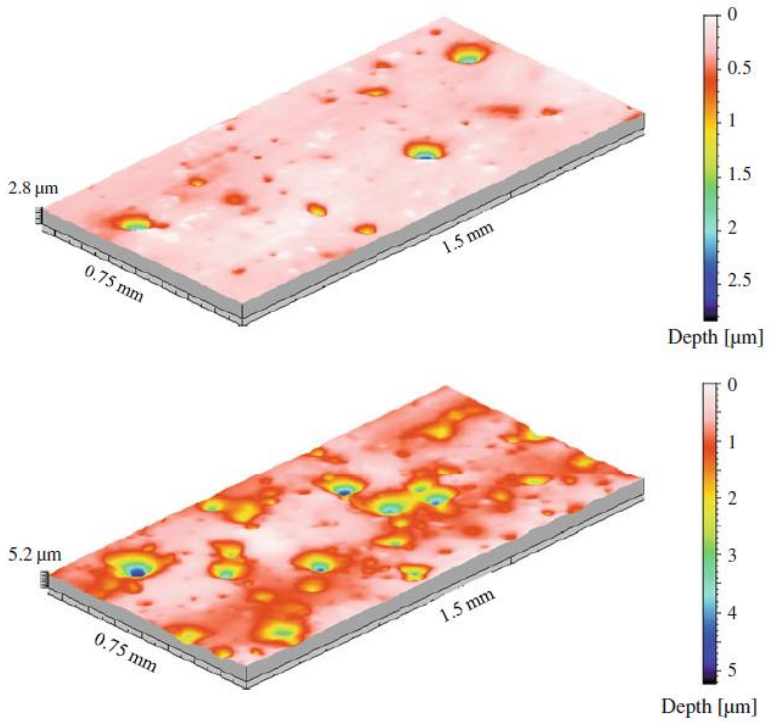

Fig. 21: Results of the pitting test performed in the cavitation tunnel on one sample (aluminium alloy) exposed to cavitation. The difference between these two images relates to the radial location at which these images were taken [2]

Pitting tests are usually analysed by profilometry method (laser, optical) or by using a scanning electron microscope [2].

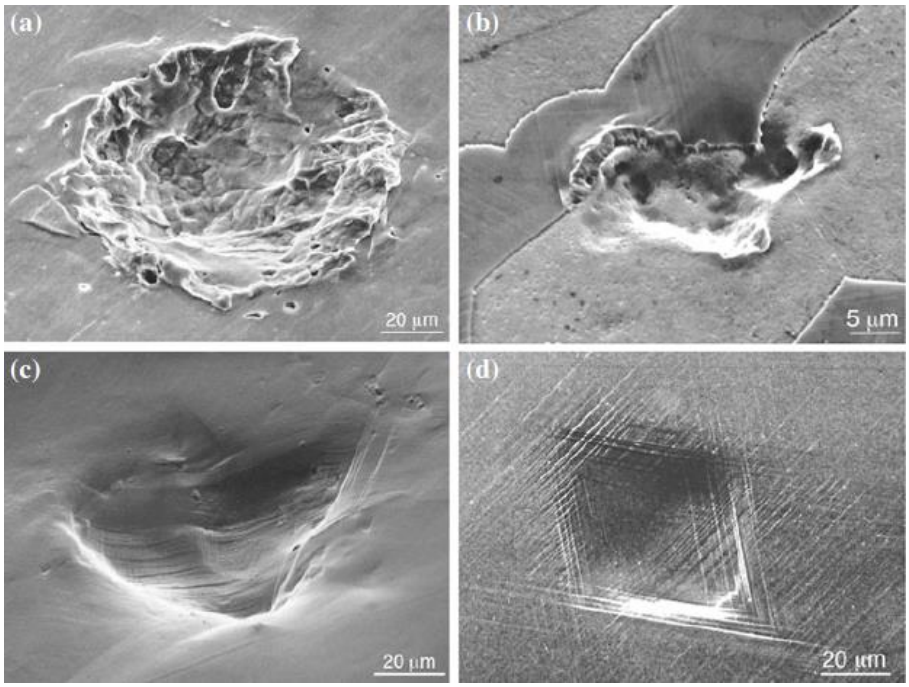

Fig 22: Images of pits resulting from cavitation on various materials taken by a scanning electron microscope, a) brass, b) duplex stainless steel, c) austenitic steel, d) Al-Cu alloy [2]

In the *acceleration (accumulation) period*, large cracks spread at the grain boundaries of the material and thus leading to the removal of microscopic fragments of the material. The mass loss curve depends not only on the type of material (its strain-hardening properties) but also on its previous processing [2].

The *deceleration (attenuation) period* starts when the surface characteristics change so much that an interaction between cavitation process and the eroded surface emerges. A significant change in the dynamics of the cavitation process occurs. Gas and liquid get entrapped in the craters on the surface, which results in weakening of cavitation pressure waves [2].

In the *steady-state (terminal) period*, the intensity of cavitation and mass loss of material is balanced. The volume loss rate is therefore almost constant and the S-curve is nearly linear in this stage. Some materials, such as elastomeric coatings, do not attain a steady state at all, because they can be delaminated or overheated, or even fail before reaching this state [2].

The first three stages are very dynamic and unsteady, so that it is quite hard to observe them in detail and describe the behaviour of various materials [2].

3.2.4 Pitting tests and their analysis [2]

As mentioned above, pitting tests are usually performed to determine the cavitation intensity. It is essential to obtain values of impact pressures produced by collapsing bubbles as they are probably the most important parameters of the cavitation intensity. These impact loads can be either measured by various pressure sensitive transducers (but despite the progress in this field, the measured values are still not completely accurate), or they can be indirectly calculated from the pits' dimensions. Except for the dimensions of the pits, stress-strain curves of the material are needed. The curves can be determined from nanoindentation tests[6].

Assuming the shape of the pit is spherical (which is a simplification as the pits are never entirely spherical), the surface load can be calculated from the maximum strain (on the surface, see Fig. 23) and stress-strain relations. For the maximum strain the following approximate equation was determined:

$$\varepsilon_{\max} \cong (\theta + 1) \cdot 0.8 \cdot \frac{h}{D}, \tag{3.7}$$

where h is the pit depth, D is the pit diameter and θ is the pit diameter obtained from the nanoindentation test.

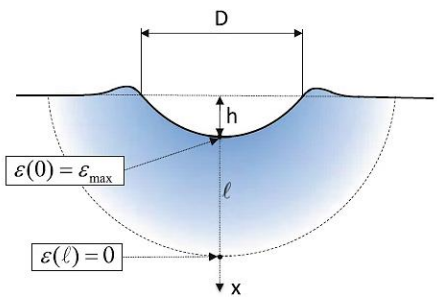

Fig. 23: The simplification of the pit and its description [2]

[6] During the nanoindentation test, a spherical nanoindenter is pressed on a surface; the acquired load-displacement curve is afterwards recalculated to obtain the stress-strain curve of the material similarly as in case of the tensile test. The advantage of the nanoindentation test is that the surface is being compressed alike during cavitation collapse [2].

It is important to note that the stress in pits is not uniaxial but triaxial, hence the equivalent (Von Mises) stress has to be evaluated to determine whether the material will exhibit the plastic deformation. In case of the rigid body only a normal stress (uniaxial stress) exists as the rigid body cannot deform and no shear forces are generated. On the other hand, real samples can deform and consequently the pressure waves deflect when they reach the pit, so that shear stresses occur (triaxial stress-state). It is the reason why there is such a big difference when normal stresses at real samples and rigid body are compared (see Fig. 23).

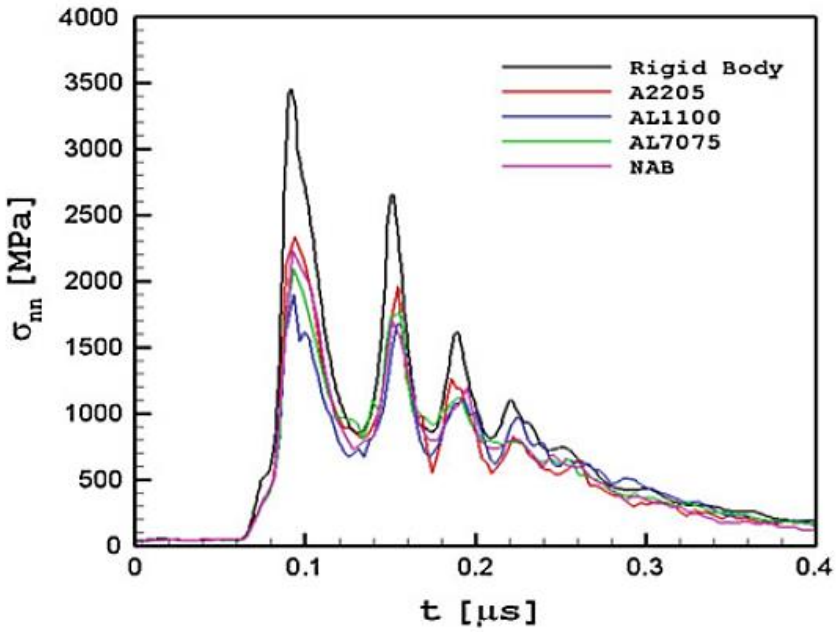

Fig. 24: A computational model of normal stresses acting on the first element below the surface of the plate; the bubble in the model was imposed to a pressure of value 5 MPa [2].

4 Methods of cavitation testing [2]

The most commonly used laboratory testing methods and equipment include the vibratory cavitation apparatus, cavitating liquid jets and high-speed cavitation tunnels.

4.1 The vibratory cavitation apparatus (ASTM G32)

This method uses magnetostrictive ultrasonic horn to generate ultrasonic waves and consequently acoustic (ultrasonic) cavitation. There are two variants of this method – direct one and alternative one.

The vibratory apparatus usually operates at frequency 20 kHz and the amplitude of the horn tip motion is 25 μm. The high frequencies of the ultrasound waves generate pressure waves, which lead to the oscillation of liquid - cyclic formation of low and high pressure occur. For the aforementioned values the amplitude of the generated pressure reaches the value of around 4.7 MPa, which is much larger than the pressure in the surrounding liquid. In the negative pulse cycle, this value is significantly lower than the critical pressure for most liquids.

In the direct method the sample is fixed to the end of the horn. A hemispherical cavitation cloud is formed; it grows and afterwards collapses. The erosion occurs thereby mostly in the centre of the sample. The process is very dynamic.

In the alternative method the sample is placed below the horn, typically in the distance around 0.5 mm. In this case, the cavitation cloud has a cylindrical shape. As a result, the eroded area is extended over the entire sample.

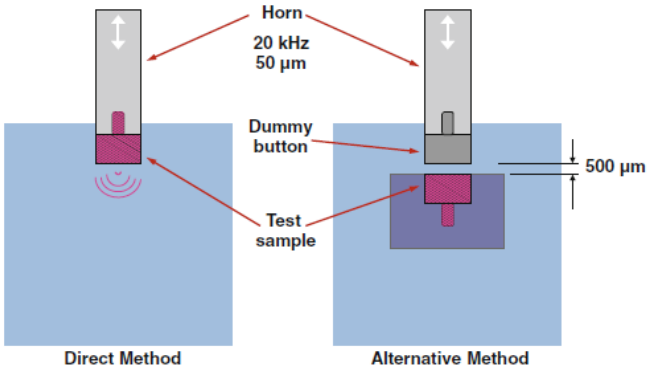

Fig. 25: Direct versus alternative method [2]

Fig. 26: Eroded area on the aluminium alloy sample – direct method (left) and alternative method (right) [2]

In both of the methods the sample is subjected to cavitation for a certain period of time, then the test is interrupted to measure the loss of the material. Then the sample is returned to the same position and again exposed to cavitation for another period of time. The result of the test is the mass loss versus time diagram.

The negative fact is that the cavitation generated in this test is different from the real one. The cavitation bubbles are almost of the same size, the method uses the same fixed frequency, there are no influences of vortices or liquid flow and the bubble cloud rises always at the same location.

4.2 Cavitating liquid jets (ASTM G134)

In this method, the cavitation occurs in the turbulent layer generated by the fast-moving liquid jet. The cavitation bubbles are usually quite randomly distributed (the so-called unstructured cavitating jets), but with a suitable change in the shape of the nozzle, they may be more organized (the so-called structured cavitating jets). The structured cavitating jets are more intense.

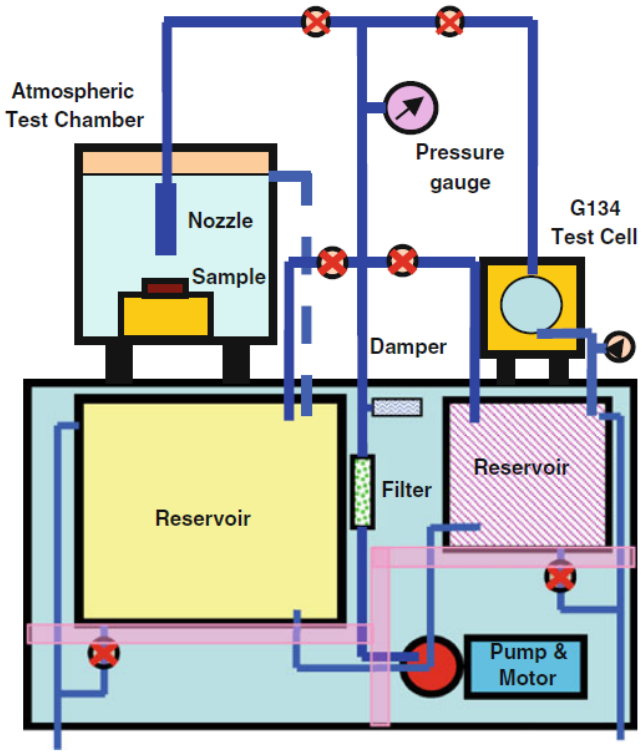

Fig. 27: The assembly of the test device [2]

The test equipment consists of two reservoirs and one pump. There is always only one tank in the operation, the other is closed by a valve. There are two loops - the left one includes a test chamber, a cavitating nozzle, a sample holder, a reservoir and a pump; the right one consists of a cavitating nozzle, a sample holder, a test cell, a reservoir and a pump. Pressure of the jet is controlled in the test cell.

The test itself proceeds in the same way as in the vibratory apparatus method and again the result of the measurement is the mass loss versus time diagram.

The advantage of the cavitating liquid jets method is that the cavitation intensity can be adjusted - for example, by changing the jet velocity or its diameter and angle. As a consequence, it is possible to obtain more realistic cavitation in comparison with the cavitation generated by the vibratory apparatus. The pressure of the jet can reach values up to 300 MPa and the cavitation number is much smaller than 1.

4.3 High-speed Cavitation Tunnels

In high-speed cavitation tunnels it is possible to reach high velocity of the flow (around 90 m s^{-1}) and consequently also high pressure (around 4 MPa), which leads to the greater intensity of the cavitation. It is convenient to use this method in case of resistant materials, as the aggressiveness of the cavitation makes the testing duration quite reasonable.

An important part of the device is the pressurization bottle, which serves to control the cavitation number. The change in the cavitation number leads to a change in cavitation intensity and consequently cavitation erosion.

Tunnels with a radial divergent section (see Fig. 28 left) are often used. The fluid is inlet in the axial direction, but then it is distributed in the radial direction along the sample.

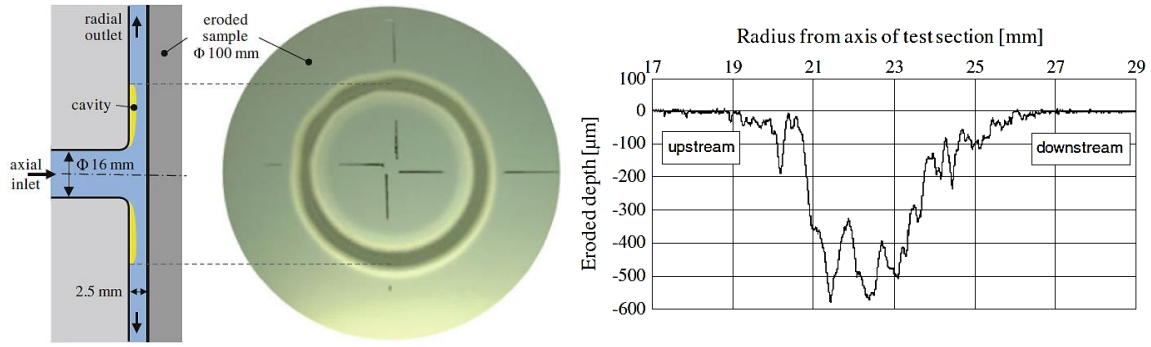

Fig. 28: A scheme of radial divergent section; cavities are formed symmetrically to the axial inlet and consequently cause an annular shaped deformation *(left)*; the picture *on the right* shows an example of a profile of the eroded area on the sample [2].

The output of the test can be the course of the profile of the eroded area in the radial direction - profilometry (see Fig. 28 right).

Recently, profilometry has come to the forefront. This method is more accurate in comparison with the method of measuring mass before and after cavitation. This is due to the fact that during the test the samples can be covered with a layer of oxides that are relatively heavy. As a consequence, the mass measured after cavitation can be higher than before cavitation, which is, of course, a nonsensical result.

5 Experimental part

5.1 Introduction

In the experimental part, specimens manufactured by various 3D printing methods were tested in terms of cavitation erosion. The plastic and metal samples were exposed to hydrodynamic cavitation in two types of tests – cavitating jet and cavitation induced by an orifice. The 3D printed metal samples were also compared with the cast specimens. Results were evaluated by surface topography and profilometry.

International research shows that there might be a potential in using 3D printing methods for manufacturing parts of hydraulic machines. Although the results are quite promising, there is still very little known in this field and not many teams examined these issues so far.

5.2 Motivation for the experimental part – international research

A team from Zhejiang University [21] dealt with an effect of the surface topography on cavitation erosion rate of alloy AlSi10Mg. Four types of surface finishing were used – turning, grinding, polishing and laser texturing (using Selective Laser Melting – SLM, see Chapter 5.3.1). Samples were exposed to cavitation in the test rig according to ASTM G134 standard. It was found out that the laser textured sample reached the highest cavitation erosion rate. Two possible explanations were given. Firstly, the laser textured sample had the biggest surface roughness, so that it was more susceptible to the inception of cavitation (according to [22]). Secondly, it is very likely that some patterns on the surface, caused by the type of manufacturing, influenced the cavitation erosion rate. However, in the steady state period the erosion rates were almost the same for all of the samples [21].

The same team continued studying the cavitation erosion of the alloy AlSi10Mg manufactured by SLM [23]. Different laser speeds were used and these samples were mutually compared and also compared with a wrought sample. All the samples were polished, so that the influence of the surface topography was reduced. According to [24], the AlSi10Mg samples produced by SLM have very fine cellular-dendritic structure, which leads to high hardness (and also high erosion resistance). However, the SLM samples have also many pores, so that the density of the sample is worsened. The team from Zhejiang University has found out that at the beginning of the cavitation erosion test (ASTM G134), the SLM samples showed a big mass loss. It was probably caused by the removal of unmelted particles in pores [23]. Nevertheless, in the steady state period the erosion rate was very low (1/10 in comparison with the wrought sample).

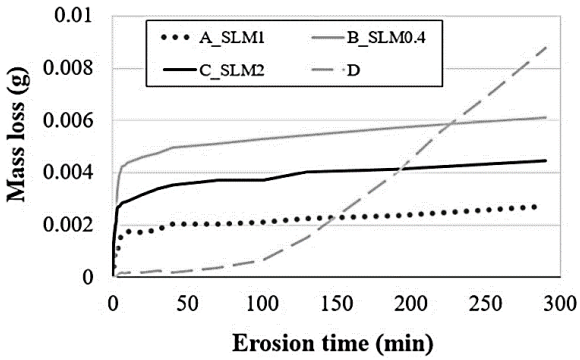

Fig. 29: The comparison of mass loss versus time diagrams of four types of samples; legend: A_SLM1 – SLM method using standard scanning speed, B_SLM0.4 – SLM using low laser speed, C_SLM2 – SLM using high laser speed, D – the wrought sample [23]

Another team from University of Brescia [25] examined the cavitation erosion of the AlSi10Mg alloy. The samples were manufactured by DMLS method (Direct Metal Laser Sintering), which is basically the same as the SLM method. These additive samples were compared with cast ones. The influence of the T6 heat treatment[7] and the hot isostatic pressing (HIP)[8] was also investigated. The samples were tested according to the ASTM G32 and outstanding results were obtained. The DMLS samples showed first mass loss signs after 40 min, the cast ones already after 16 min. The total mass loss during 8 hours of testing of DMLS samples was about 88% less than in case of the cast samples. The T6 treatment worsened the result in case of the DMLS samples, as the fine structure was affected and hardness was reduced. On the other hand, the T6 treatment led to better results in case of cast samples [25].

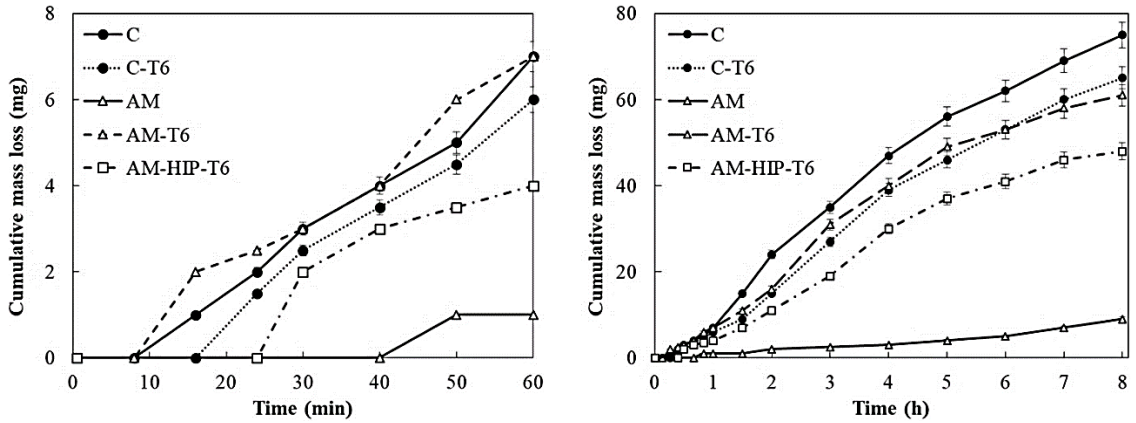

Fig. 30: Both pictures show mass loss versus time curves; legend: C – cast samples, C-T6 – cast samples after the T6 treatment, AM – additive manufacturing samples, AM-T6 - additive manufacturing samples after the T6 treatment, AM-HIP-T6 - additive manufacturing samples after the HIP and the T6 [25]

A team from The Hong Kong Polytechnic University [26] examined the cavitation erosion of manganese-nickel-aluminium bronze (MAB) and nickel-aluminium bronze (NAB), which are often used as a marine propeller alloy. The surface layer was altered by LSM method (Laser Surface Melting), which led to a fine and homogenous structure of the surface. This better structure (in comparison with the untreated samples) together with increased hardness of the materials provided increased cavitation erosion resistance [26].

[7] T6 heat treatment has two phases: 1) quenching, 2) ageing and hardening phase [27].

[8] HIP is a procedure that uses high pressures and temperatures to obtain isotropic properties and higher density of the samples [28].

5.3 Materials and manufacturing methods

5.3.1 Manufacturing methods of the samples

The plastic samples were manufactured by FDM and PolyJet method, the metal ones by SLM method.

FDM (Fused Deposition Modeling)

In this method, thermoplastic polymers in a form of filaments are used. The filaments are led to an extrusion head by feeds and afterwards they are being melted in a nozzle and deposited layer-by-layer on the prepared worktable. The products are usually very durable. It is probably the most often used method of 3D printing [29].

PolyJet

This method uses photopolymer resins, which are melted in a nozzle. The thin layers (respectively droplets) of the melted material are deposited on the worktable and afterwards they are cured by UV light. The PolyJet method enables printing of detailed objects and the consequent surface is smooth [30].

SLM (Selective Laser Melting)

This method is used for 3D printing of metals. As a result of high temperatures and a full melting process, a homogenous structure is reached, which leads to better physical properties of the object. The procedure has to be run in a special chamber filled with an inert gas (argon or nitrogen). A layer of the metal powder is laid on the worktable and the laser sinters it according to the data in the 3D file. Afterwards, the worktable drops a little bit before the new layer is applied [31].

5.3.2 Materials

The metal materials used in the experiment are listed in Table 1, the plastic ones in Table 2.

Table 1: Material characteristics of cast stainless steel 316L (*source: IPM CAS*), cast alloy AlSi10Mg [32], SLM stainless steel and SLM alloy AlSi10Mg (*source: DREAT BUT)*

Material	Yield strength Rp0,2 [MPa]	Ultimate strength Rm[MPa]	HRB
Stainless steel 316L (cast)	449	639	92
Alloy AlSi10Mg (cast)	240	460	68
Stainless steel 316L (SLM)	505	620	-
Alloy AlSi10Mg (SLM)	237	400	-

The specific material characteristics for the cast alloy AlSi10Mg were impossible to obtain, but it is known that it was as received (without heat treatment) alloy, so that the characteristics for this alloy presented in Table 1 are approximate values obtained at the internet website [32] just for an idea.

Table 2: Material characteristics of the plastic materials [33], [34]

Material	ABS	Nylon12	ULTEM 9085	Antero 800NA	PolyJet VeroClear
Printing method	FDM	FDM	FDM	FDM	PolyJet
Tensile yield strength [MPa]	26	28	33	46	50 - 65
Tensile modulus [MPa]	2180	1138	2270	3500	2000 - 3000
Compressive yield strength [MPa]	-	55	87	101	-
Compressive modulus [MPa]	-	1069	1731	2300	-

Short characteristics of each plastic material [34]*:*

ABS – thermoplastic, which is often used for strong and stiff components

Antero 800 NA – thermoplastic with good chemical and high temperatures resistance

Nylon 12 – thermoplastic for models with a high strength

ULTEM 9085 – thermoplastic for light but also durable and strong components

PolyJet VeroClear – photopolymer resin with good tensile material characteristics

Specimens:

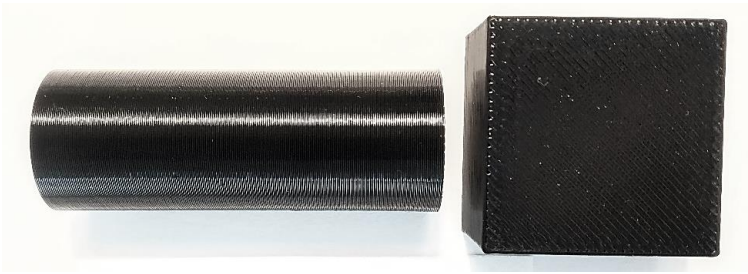

Fig. 31: Samples from material ULTEM 9085, *source: author*

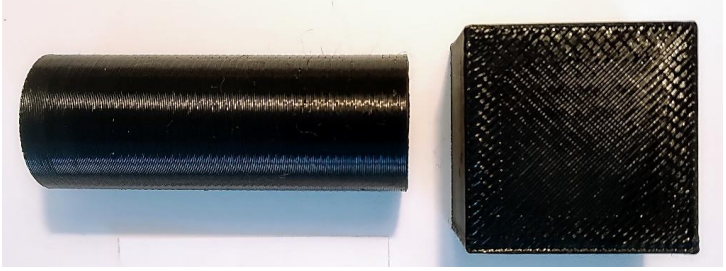

Fig. 32: Samples from material Nylon 12, *source: author*

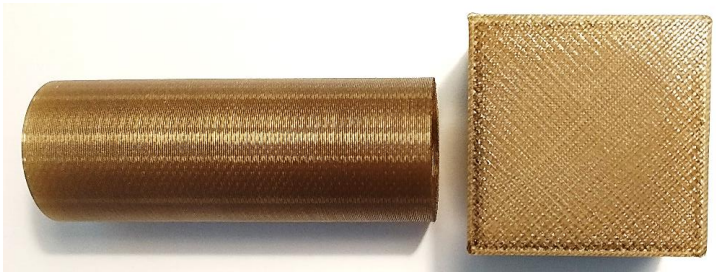

Fig. 33: Samples from material Antero 800NA, *source: author*

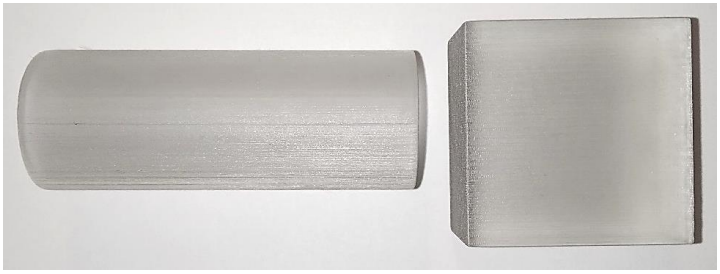

Fig. 34: Samples from material PolyJet VeroClear, *source: author*

Fig. 35: Samples from material AlSi10Mg – 3D printing *(left)*, cast one *(right)*, *source: author*

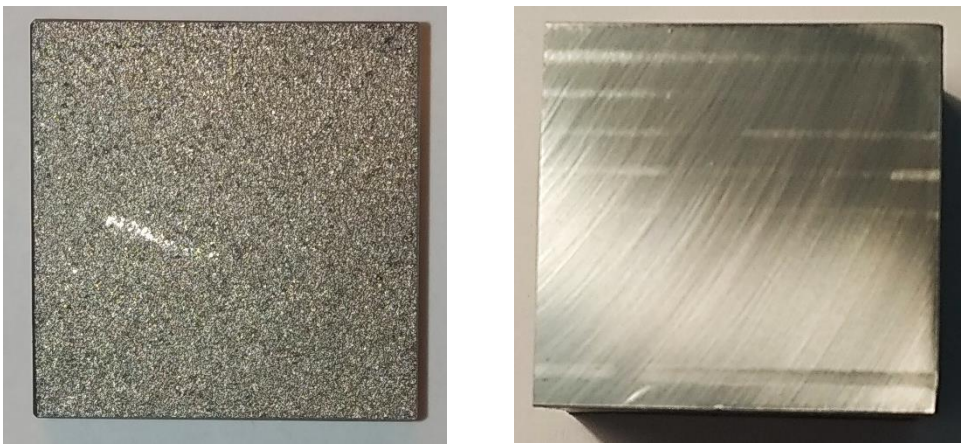

Fig. 36: Samples from steel 316L – 3D printing *(left)*, cast one *(right)*, *source: author*

Cast metal samples were polished to get a better surface roughness.

5.4 Testing methods

5.4.1 A circuit with an orifice

This method of cavitation testing is presented in Fig. 37. It contains a water circuit with an orifice (diameter 13 mm), which makes the water flow with a higher velocity (according to the continuity equation) that leads to a drop in a pressure (according to the Bernoulli equation). When a pressure drops to the saturated vapor pressure, a cavitation is incepted. A cloud of bubbles is then transported towards the sample (it is located 90 mm behind the orifice), where it collapses dynamically.

The circuit contains pipes with diameter 53 mm, a water tank, a centrifugal pump (its parameters are presented in Table 3) controlled by frequency converter, an induction flowmeter (Table 4), pressure sensors (Table 5) and a test section, which is made from plexiglass in order to observe the cavitation. The pressure sensors were placed close ahead of the orifice and behind the test section. A disadvantage of this circuit is that the cavitation number can be only adjusted through the flow rate, as the circuit is open to atmosphere and there is no vacuum pump for changing the pressure [35].

In this method only the plastic specimens were tested, as the hydrodynamic cavitation induced by the orifice is not intensive enough and it would take a long time to erode metal samples. The plastic specimens were prepared by FDM and PolyJet method in the shape presented in Fig. 38. They were threaded on a metal stick and their edges were filed away, so that they could be fitted in the test section and simultaneously prevented from rotation. Another metal stick was used to support the sample, see Fig. 39. The test lasted 16 hours for all the specimens. After 8 hours the test was stopped to make a visual control and then the testing continued for other 8 hours.

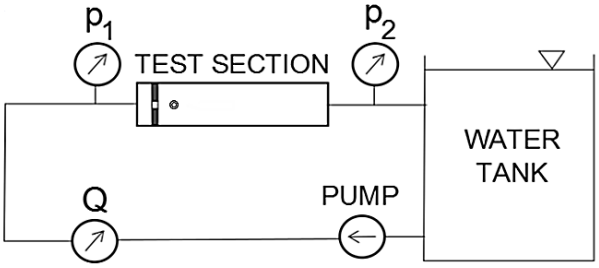

Fig. 37: A scheme of the circuit with the orifice, adapted from [35]

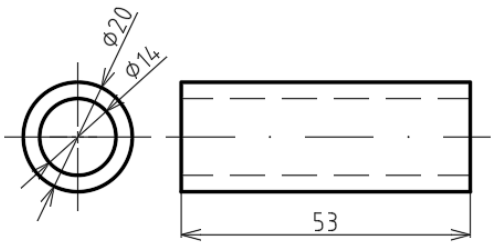

Fig. 38: Dimensions of the sample, *source: author*

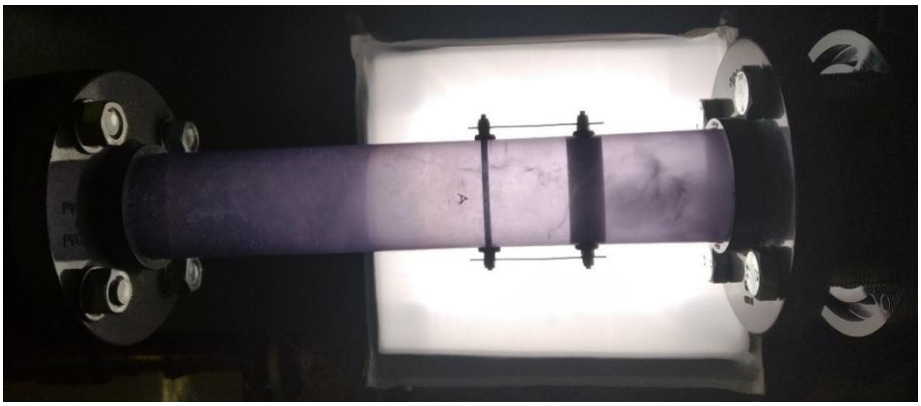

Fig. 39: A sample in the circuit with the orifice, *source: author*

Fig. 40: The whole testing circuit with the orifice, *source: author*

Used technical equipment

Water was pumped from the tank using centrifugal pump DPVSF 45-40.

Table 3: Technical parameters of the centrifugal pump DPVSF 45-40

Centrifugal pump DPVSF 45-40	
Maximum discharge	15 kW
Maximum flow rate	45 $m^3 \cdot h^{-1}$
Frequency	50 Hz

The flow was measured using induction flowmeter MQI 99 DN50 of brand ELA.

Table 4: Technical parameters of the induction flowmeter [39]

Induction flowmeter	
Principle	pulse DC
Maximum temperature of medium	90 °C
Standard pressure impact	1.6 MPa

Pressure sensors DMP 331 measured absolute static pressures in front of and behind the test section.

Table 5: Technical parameters of the pressure sensor DMP 331 of company BD SENSORS [40]

Pressure sensor DMP 331	
Range of measurement – in front of the test section (pressure p_1)	0 −16 bar
Range of measurement – behind the test section (pressure p_2)	0 − 1.6 bar

Cavitation number

Quantities measured by the technical equipment:

Pressure p_1 = 4.74 bar = 474 000 Pa

Pressure p_2 = 1.026 bar = 102 600 Pa

Temperature t = 18.8 °C

Flow $Q = 2.63\ \mathrm{l \cdot s^{-1}} = 2.63 \cdot 10^{-3}\ \mathrm{m^3 \cdot s^{-1}}$

Calculation of the saturated vapor pressure [13]:

$$p_v = 612.84 + 41.151 \cdot t + 2.012 \cdot t^2 - 0.0122 \cdot t^3 + 0.0011 \cdot t^4 = 2153.95\ \mathrm{Pa} \qquad (5.1)$$

Calculation of the cavitation number [35]:

$$\sigma = \frac{p_2 - p_v}{p_1 - p_2} = 0.2705 \qquad (5.2)$$

Cavitation number in this circuit had a value of 0.2705.

5.4.2 Cavitating jet

This method is inspired by ASTM G134 test, which was presented in Chapter 4.2. The circuit contains a piston pump, a gas accumulator for absorption of pulsations, a pressure sensor, and a nozzle with diameter 1.2 mm. The nozzle is submerged approximately 6 cm below a water level. The distance from the nozzle to a specimen is 20 mm [35].

Both plastic and metal (3D printed and cast ones) specimens were tested in this way. The metal specimens, manufactured by SLM, had the shape of a block with dimensions 30x30x3 mm, the cast ones 30x30x10-20 mm, and the plastic ones (prepared by FDM and PolyJet) were also in the shape of a block but with dimensions 30x30x20 mm. The plastic specimens have to be thicker as the cavitation intensity is quite high in this method and the materials are rather soft. The test lasted 5 min for all the plastic specimens and 90 minutes for the metal ones to comfort the standard testing at the department, see [35].

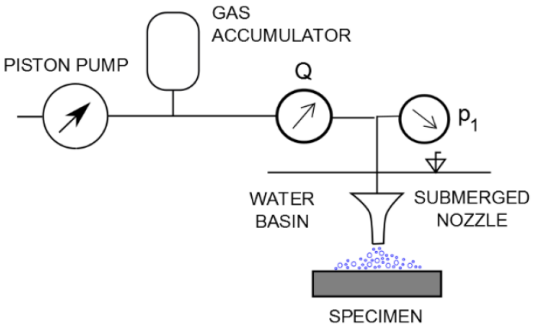

Fig. 41: A scheme of the cavitating liquid jet test [35]

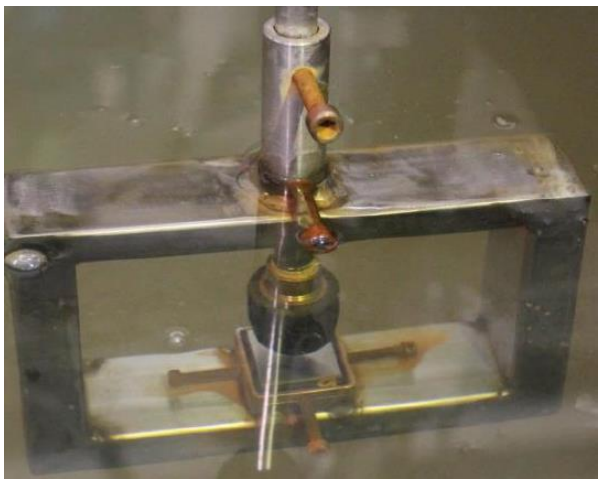

Fig. 42: The equipment for the cavitating jet test – nozzle, nozzle holder, table [35]

Used technical equipment

Water was pumped by piston pump INTERPUMP E2B2014.

Table 6: Technical parameters of the piston pump INTERPUMP E2B2014

Piston pump INTERPUMP E2B2014	
Maximum output pressure	200 bar
Maximum flow rate	14 $l \cdot min^{-1}$
Revolutions per minute	1450

The pressure was measured by manometer WIKA.

Table 7: Technical parameters of the manometer WIKA

Pressure sensor DMP 331	
Range of measurement	0−250 bar
Class of accuracy	2.5

Cavitation number

Pressure $p_{1,\,abs}$ measured by the pressure sensor behind the pump (respectively ahead of the nozzle): $p_{1,\,abs}$ = 180 bar

Pressure $p_{2,\,abs}$ in the water tank: $p_{2,\,abs}$ = 1 bar (≈ atmospheric pressure)

Flow through the nozzle, calculated from the nozzle catalogue [41]: 12.58 l/min

Calculation of the cavitation number:

$$\sigma = \frac{p_{2,abs}}{p_{1,abs}} = 0.00\bar{5} \tag{5.3}$$

In this test the cavitation number has a significantly lower value than in the circuit with the orifice, thus in this test the cavitation is more aggressive and its intensity is much higher.

5.5 Results

5.5.1 Results from the circuit with the orifice

Despite the fact that the plastic specimens were subjected to cavitation for 16 hours, there was no visible damage. The reason is probably the low cavitation intensity and damping properties of the plastic materials.

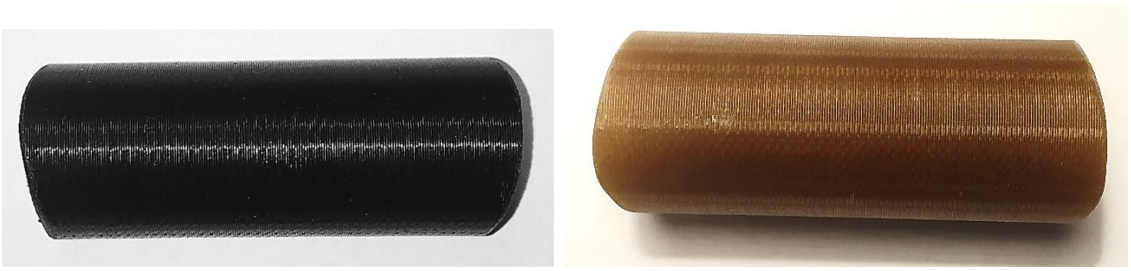

Fig. 43: Nylon 12 *(left)* and Antero 800NA *(right)* after the test, *source: author*

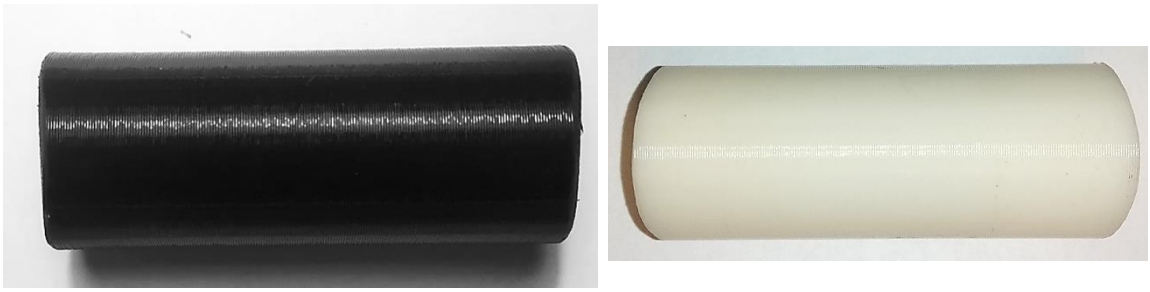

Fig. 44: ULTEM 9085 *(left)* and ABS *(right)* after the test, *source: author*

Fig. 45: PolyJet VeroClear after the test, *source: author*

The apparent erosion can be observed only on PolyJet VeroClear (but still not a significant one). The surface became more rough and individual ligaments of the material exhibit a slight waviness in comparison with other specimens. The higher erosion damage of the PolyJet VeroClear specimen might be related to the material characteristics but also to the orientation of the ligaments – in this case they are oriented in the axial direction while the ligaments in other specimens were printed in circumferential direction, which can result in a lower erosion rate. The effect of ligament orientation would likely deserve further examination.

5.5.2 Results from the cavitating jet test

5.5.2.1 Plastic samples

Antero 800NA

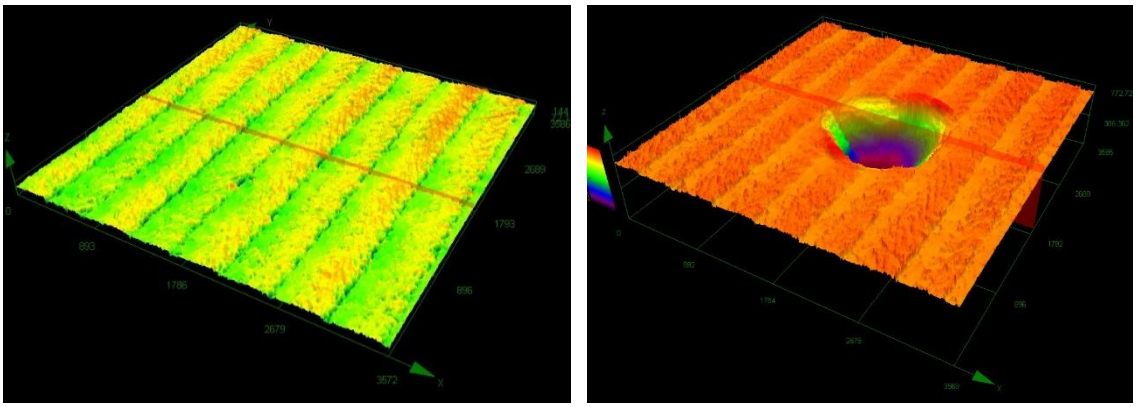

(a) (b)

Fig. 46: Surface topography of plastic material Antero 800NA before the test (a) and after the test (b), *source: CEITEC*

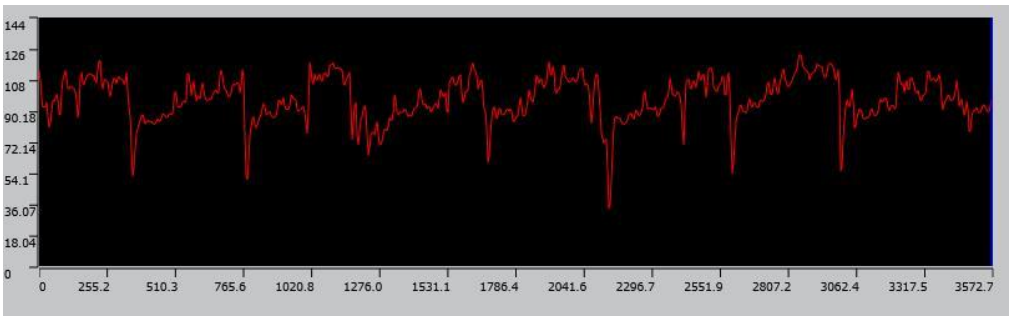

(a)

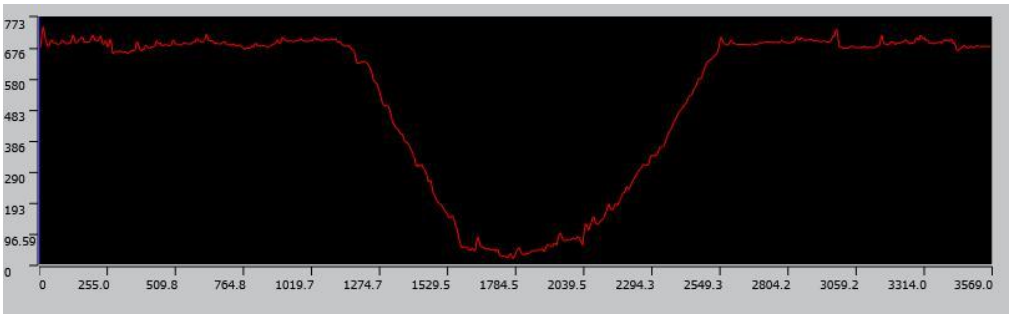

(b)

Fig. 47: Profilometry of plastic material Antero 800NA before the test (a) and after the test (b), dimensions – µm, *source: CEITEC*

All the dimensions are in micrometres. The initial roughness of the surface was around 65 µm. The cavitation impact caused a big damage to the sample, the crater in Fig. 47 (b) has depth of around 665 µm.

Nylon 12

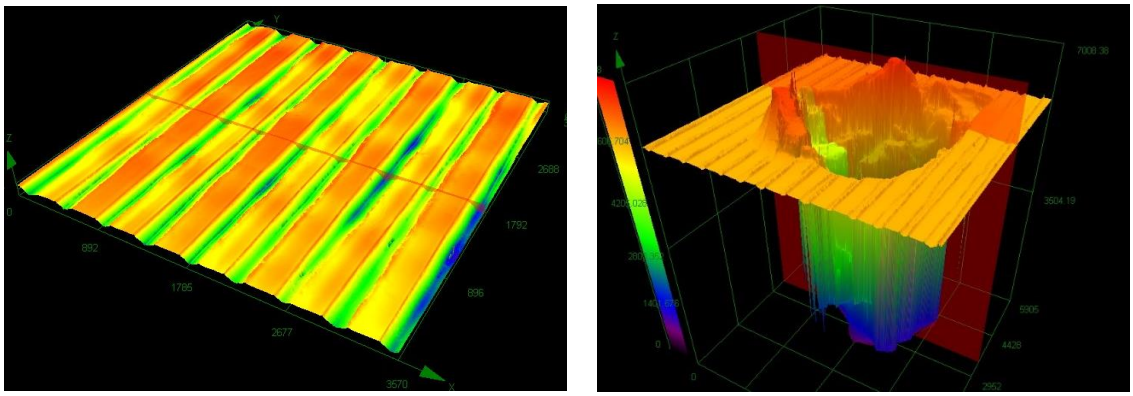

(a) (b)

Fig. 48: Surface topography of plastic material Nylon 12 before the test (a) and after the test (b), *source: CEITEC*

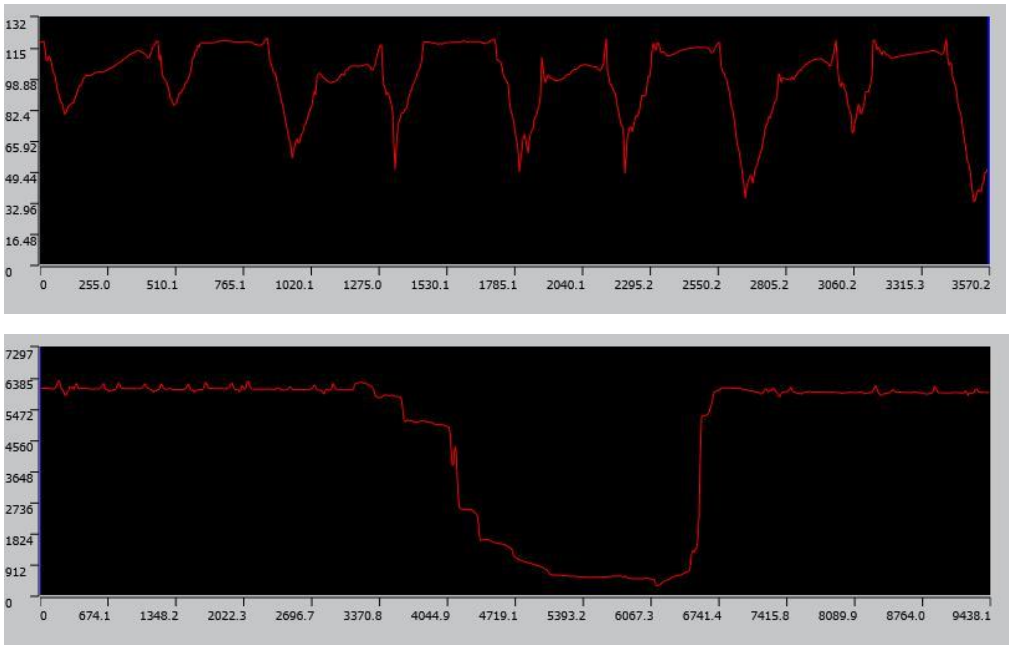

(a)

(b)

Fig. 49: Profilometry of plastic material Nylon 12 before the test (a) and after the test (b), dimensions – μm, *source: CEITEC*

In case of Nylon 12 the initial roughness was around 75 μm and the depth of the crater is around 5740 μm, thus much larger than in case of Antero 800NA. This is probably due to the higher compressive yield strength of Antero 800NA.

ULTEM 9085

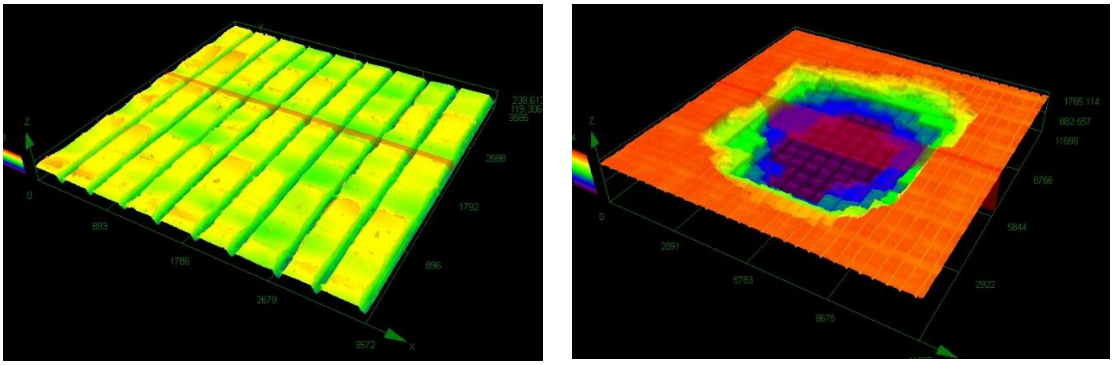

(a) (b)

Fig. 50: Surface topography of plastic material ULTEM 9085 before the test (a) and after the test (b), *source: CEITEC*

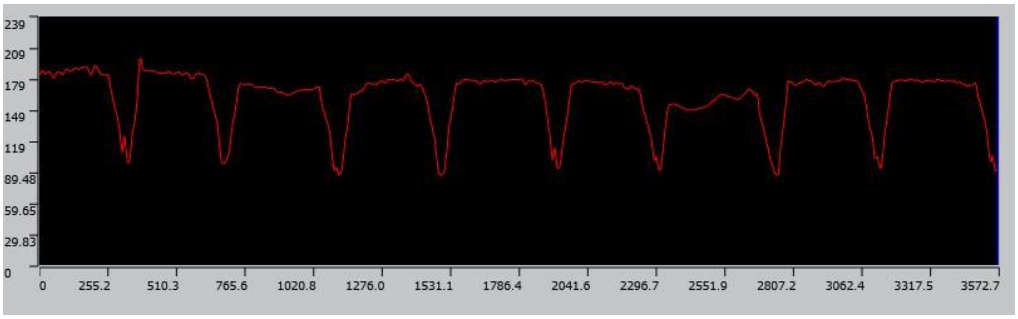

(a)

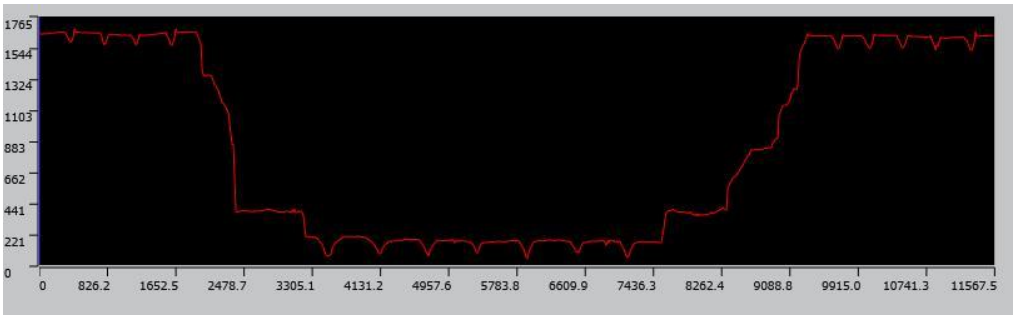

(b)

Fig. 51: Profilometry of plastic material ULTEM 9085 before the test (a) and after the test (b), dimensions – μm, *source: CEITEC*

The initial roughness was around 90 μm, after the test a big damage occurred – with the depth of approximately 1600 μm, the width of the damage is in Table 8.

PolyJet VeroClear

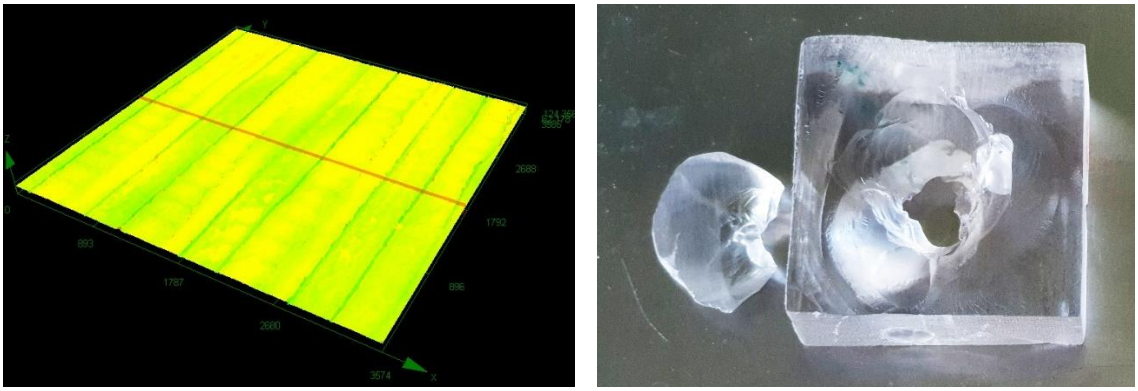

(a) – *source: CEITEC* (b) – *source: doc. Ing. P. Rudolf, Ph.D.*

Fig. 52: Surface topography of plastic material PolyJet VeroClear before the test (a) and picture of the sample after the test (b)

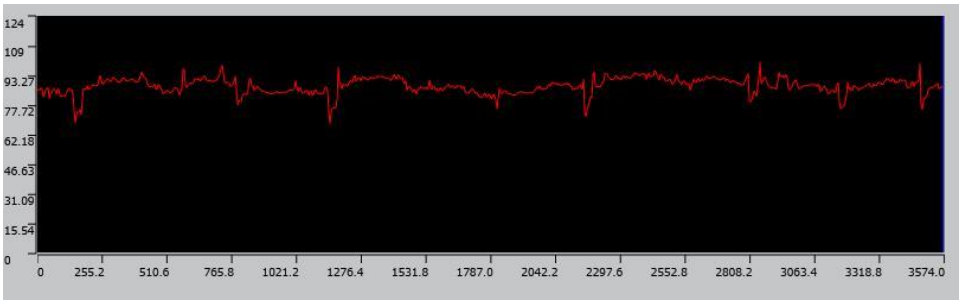

Fig. 53: Profilometry of plastic material PolyJet VeroClear before the test, dimensions – μm, *source: CEITEC*

In case of PolyJet VeroClear only profilometry and surface topography before the test are presented, as the cavitation had such a big impact on this material, that it made a hole through the whole sample and the specimen cracked into several pieces, see Fig. 52 (b). This result is quite surprising, as the material possesses quite good material characteristics (Table 2). Unfortunately, the compressive material characteristics are missing.

ABS

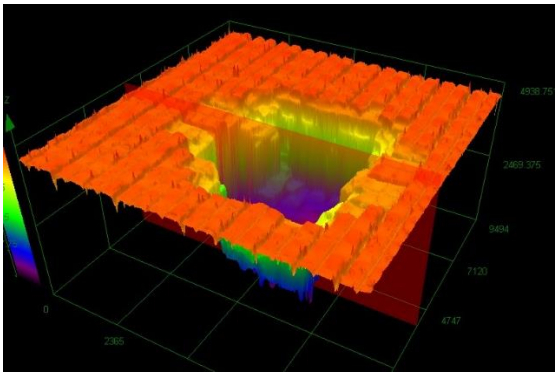

Fig. 54: Surface topography of plastic material ABS after the test, *source: CEITEC*

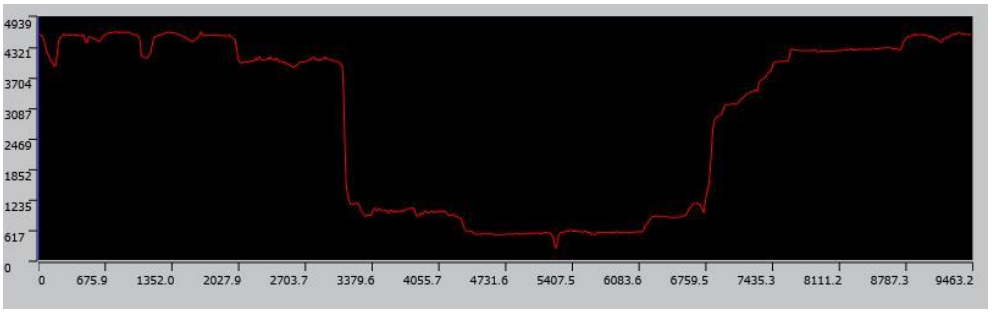

Fig. 55: Profilometry of plastic material ABS after the test, dimensions – μm, *source: CEITEC*

In case of plastic material ABS only pictures after the test are presented, as the sample was not available for the analysis before the test. Cavitation caused again a large crater in the sample – around 4200 μm.

Comparison of the plastic materials

Table 8: Dimensions of damaged parts on plastic specimens, *source: CEITEC*

Material	Width x [µm]	Width y [µm]	Depth [µm]	Approximate volume of the eroded area [mm^3]
ABS	6781.1	5989.9	4168.3	132.975
Antero 800NA	1429.8	1467.1	665.9	1.097
Nylon 12	3800.6	4794.4	5740.8	82.158
ULTEM 9085	8129.1	9809.2	1592.4	99.728

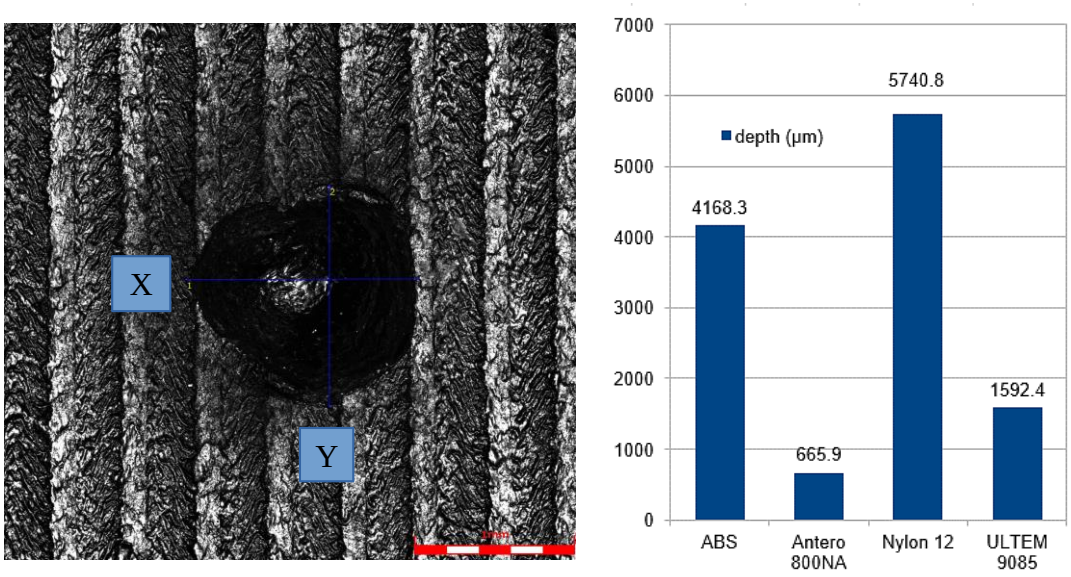

(a) (b)

Fig. 56: Directions x and y on the sample (a), comparison of depth of craters (b), *source: CEITEC*

The most serious damage was observed at PolyJet VeroClear specimen– cavitation made a hole through the whole sample. As the cavitation has a compressive impact, there seems to be a dependence of the damage level on the compressive material characteristics presented in Table 2. Unfortunately, these characteristics are missing for ABS and PolyJet VeroClear. According to both the volume and the depth of the eroded area, Antero 800NA with the highest compressive yield strength and modulus shows the best cavitation resistance. Thus it seems to be the best option (out of the tested materials) for manufacturing plastic components and armatures, which can be used in hydraulic circuits. Likely, the material might be used also for smaller submersible and garden pumps, whose impellers are made of plastic materials.

ULTEM 9085 shows the second lowest depth of the damage, but the area of the crater observed on the sample surface was quite large, thus the volume of the crater possessed the biggest value. This result is quite surprising as the material compressive characteristics are quite good. On the other hand, Nylon 12 with worse material compressive characteristics was not eroded so much. A possible explanation for the large surface area of the crater in ULTEM 9085 is a strongly heterogeneous material structure with ligaments weakly bonded together, hence the material characteristics valid for ligaments cannot be extended for the whole specimen. Moreover, it is likely that the cavitation intensity in this test was too high, therefore the obtained results might not be entirely reliable. More tests with lower cavitation intensity should be conducted to make a proper conclusion. .

5.5.2.2 Stainless steel 316L

Stainless steel 316L – 3D printed

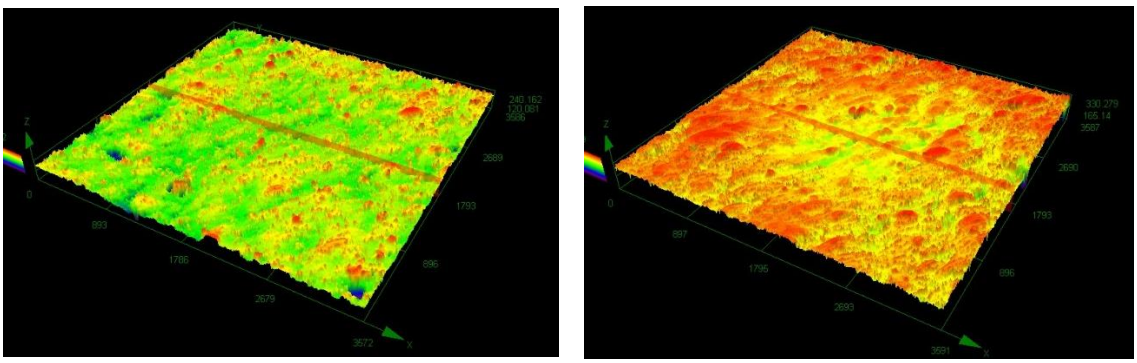

(a) (b)

Fig. 57: Surface topography of stainless steel 316L (3D printed) before the test (a) and after the test (b), *source: CEITEC*

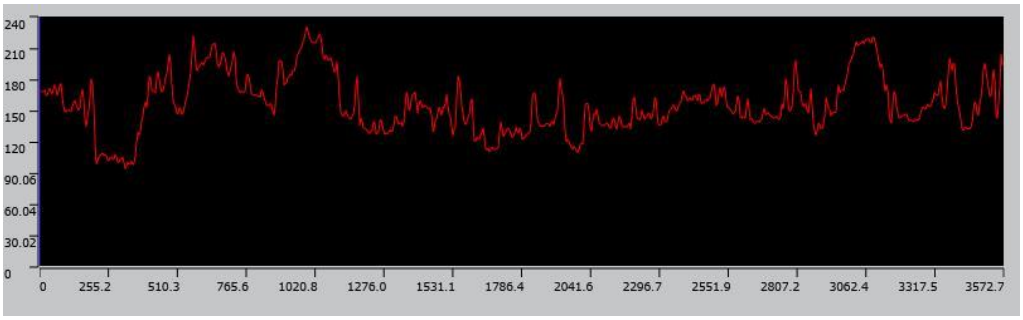

(a)

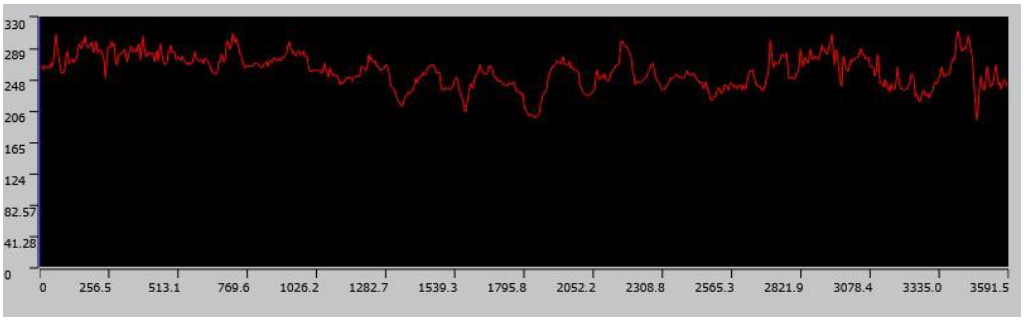

(b)

Fig. 58: Profilometry of stainless steel 316L (3D printed) before the test (a) and after the test (b), dimensions – µm, *source: CEITEC*

The roughness of the 3D printed stainless steel 316L slightly changed during the experiment (the initial roughness was around 150 µm and after the test around 130 µm). Surprisingly, the surface looked smoother after conducting the experiment, see Fig. 58 (b). It suggests that the surface grains, which were not melted properly and consequently weakly connected to the bulk of material, form "hills", thus significantly contributing to the surface roughness. Likely, they were released from the material during the experiment, thus reducing the apparent surface roughness. Strangely, after the test the maximum peak was higher (around 310 µm) than before the test (around 240 µm). It is possible that a thin layer of oxides was created on the surface.

Stainless steel 316L – cast

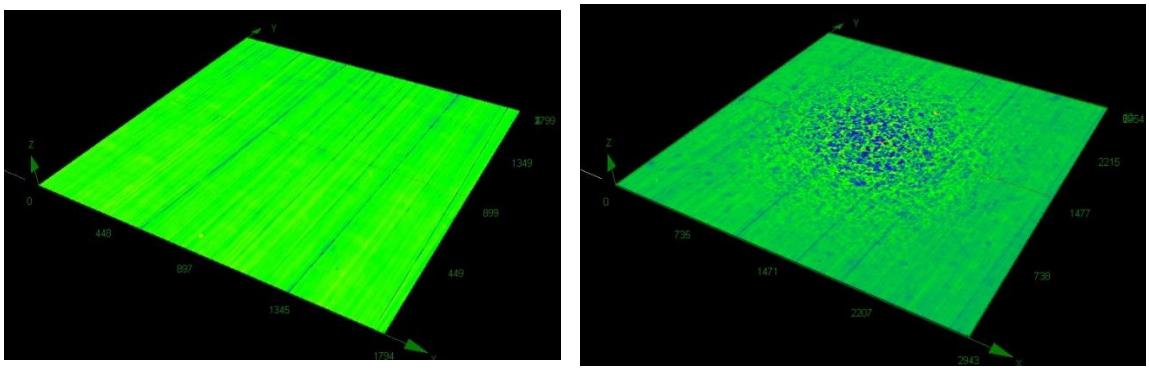

(a) (b)

Fig. 59: Surface topography of stainless steel 316L (cast) before the test (a) and after the test (b), *source: CEITEC*

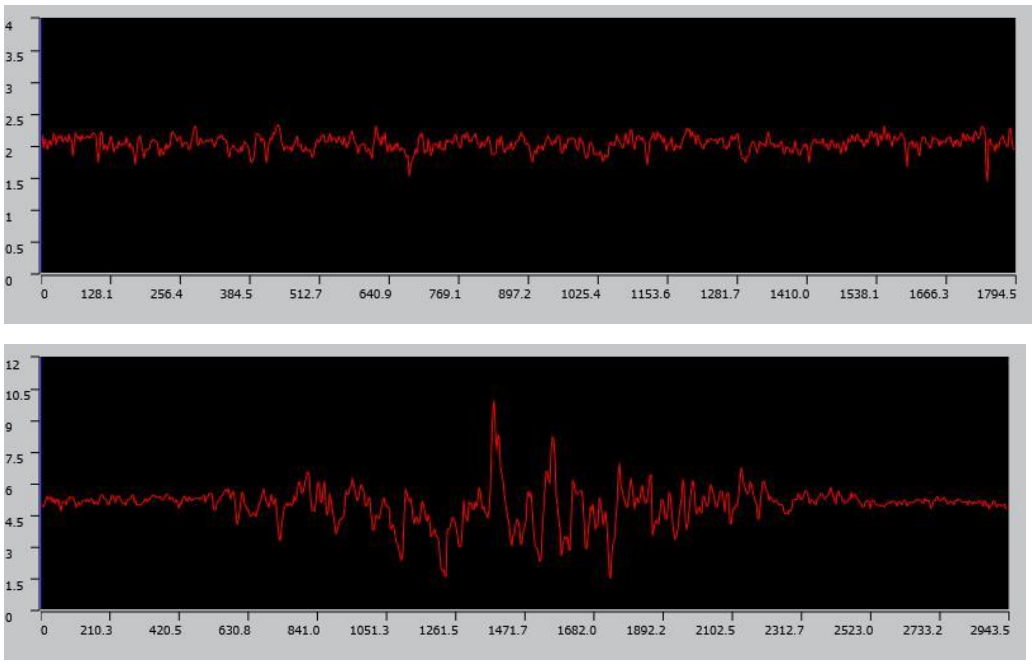

(a)

(b)

Fig. 60: Profilometry of stainless steel 316L (cast) before the test (a) and after the test (b), dimensions – μm, *source: CEITEC*

The cast stainless steel has much lower initial roughness (around 0.75 μm) than the 3D printed one. After the experiment the surface became significantly rougher – maximum is around 9 μm.

Comparison of the 3D printed and cast stainless steel 316L

It is quite hard to decide which manufacturing method is better in case of stainless steel 316L, as their initial roughness was very different. However, it can be said, that the 3D printed one showed less percentual change than the cast one. The problem that can occur with the 3D printed sample is a segregation of alloy elements at grain boundaries because of high temperatures during SLM manufacturing.

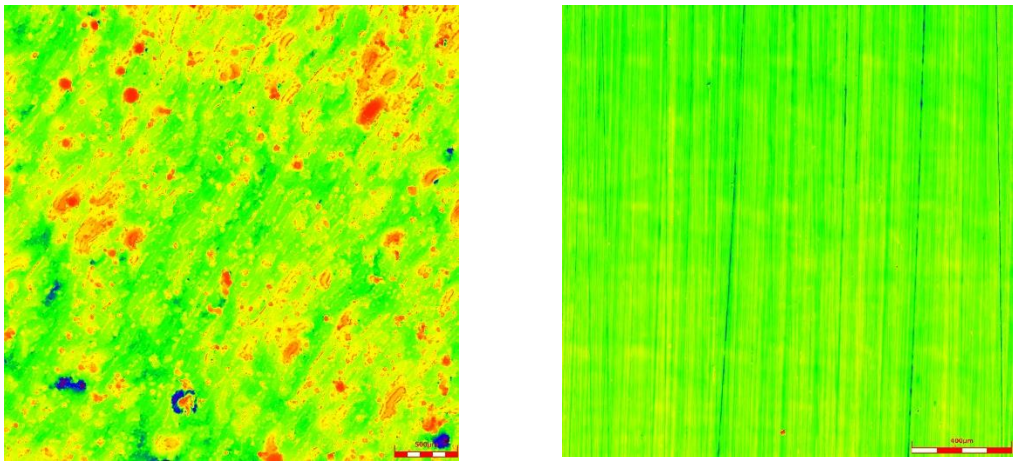

(a) (b)

Fig. 61: A structure of the 3D printed stainless steel (a) and cast one (b) before the test, *source: CEITEC*

In case of 3D printed stainless steel, pores and molten pools can be observed in the structure. Laser in SLM method produces temperature of around 2000 °C impacting a small spot (diameter of approximately 50 μm). However, the scanning speeds are quite high (hundreds to thousands of mm/s), so that the material cools down quite quickly and a significant temperature gradient occurs [23]. This leads to a special structure of the 3D printed materials, which is different from the conventionally produced (cast or wrought) one, see Fig. 61. However, as mentioned above, segregation of alloys can occur, thus the mechanical characteristics might be worsened.

Further tests should be conducted to determine which manufacturing method is more suitable. Same (or very similar) initial roughness of cast and 3D printed would be needed to make a proper comparison.

5.5.2.3 Aluminium alloy AlSi10Mg

Aluminium alloy AlSi10Mg – 3D printed

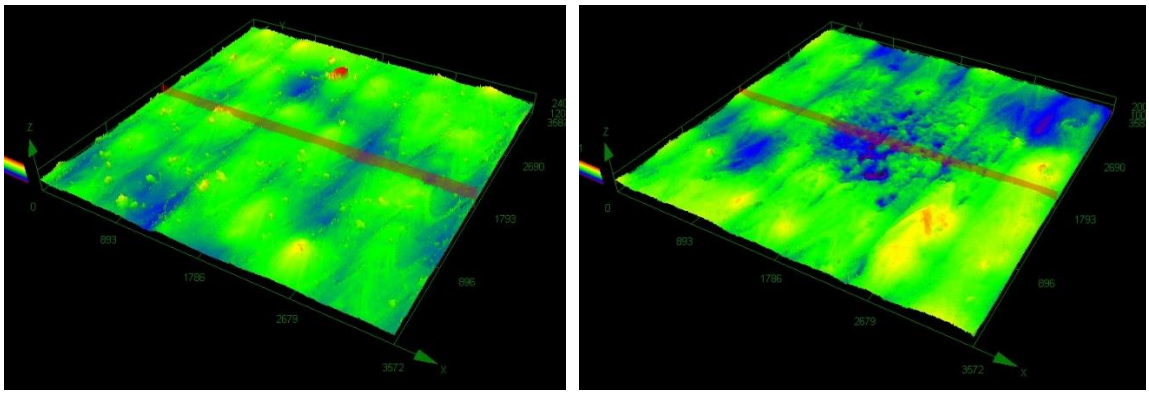

(a) (b)

Fig. 62: Surface topography of aluminium alloy AlSi10Mg (3D printed) before the test (a) and after the test (b), *source: CEITEC*

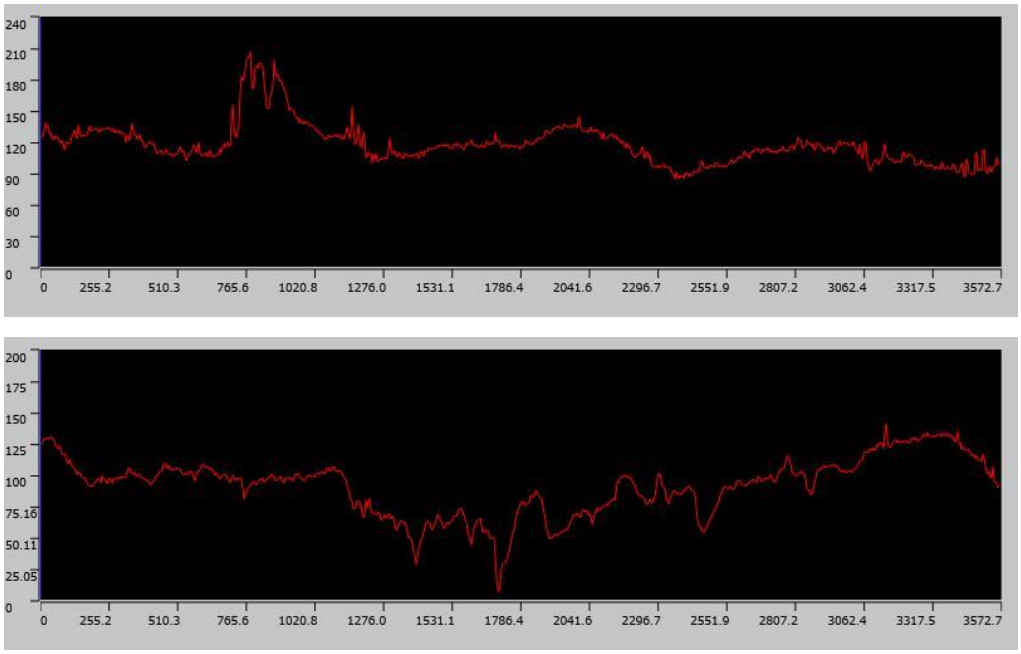

(a)

(b)

Fig. 63: Profilometry of aluminium alloy AlSi10Mg (3D printed) before the test (a) and after the test (b), dimensions – µm, *source: CEITEC*

Initial roughness of the sample was around 120 µm and after the test approximately 140 µm, which indicates that the percentual change of the roughness is relatively small in comparison with the cast AlSi10Mg sample, see the next Figure.

Aluminium alloy AlSi10Mg – cast

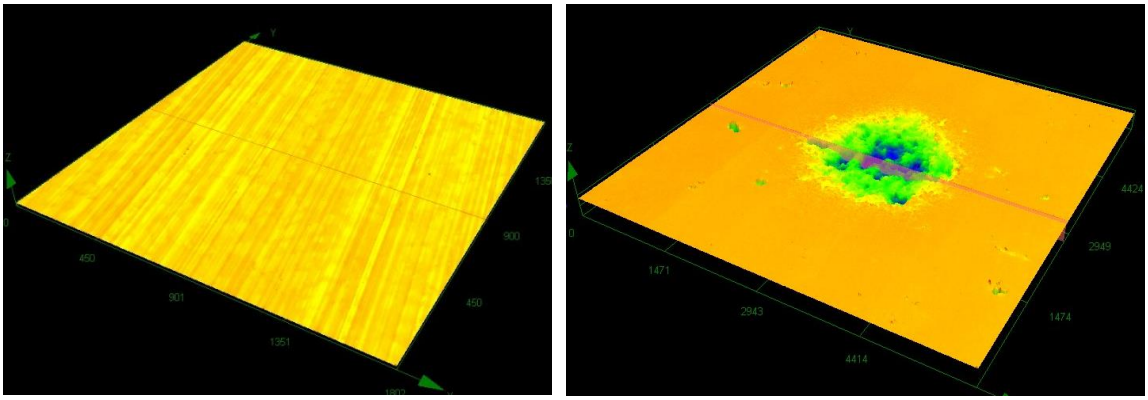

(a) (b)

Fig. 64: Surface topography of cast aluminium alloy AlSi10Mg before the test (a) and after the test (b), *source: CEITEC*

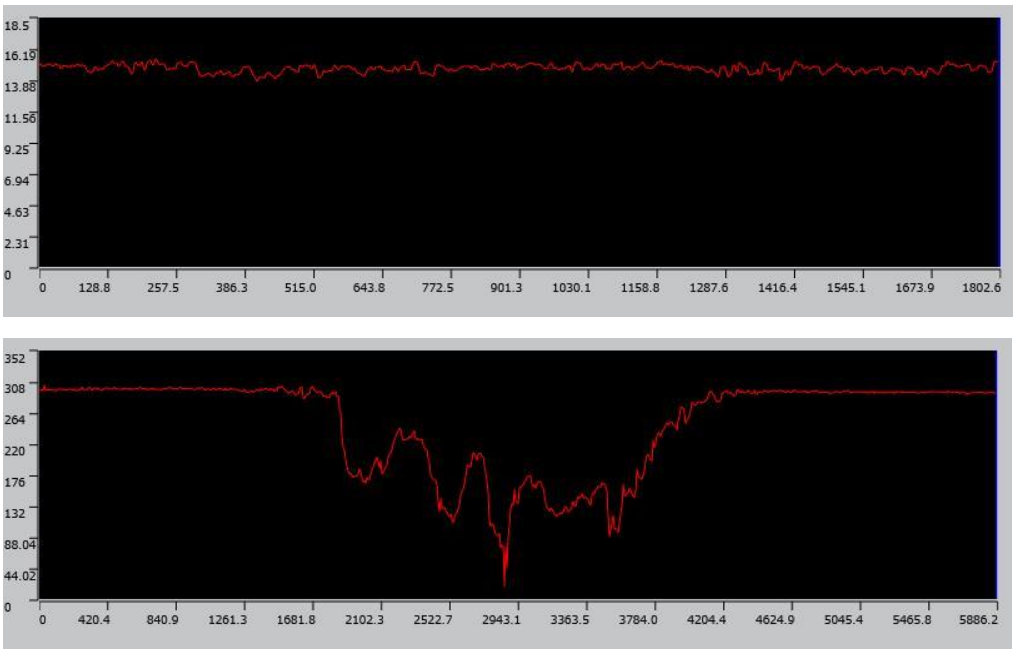

(a)

(b)

Fig. 65: Profilometry of cast aluminium alloy AlSi10Mg before the test (a) and after the test (b), dimensions – μm, *source: CEITEC*

Initial roughness of the cast AlSi10Mg sample was around 2 μm, after the test a big damage occurred – the depth of the crater in Fig. 65 (b) is around 300 μm.

Comparison of the 3D printed and cast aluminium alloy AlSi10Mg

It is evident from Fig. 63 and Fig. 65 that the cast aluminium alloy AlSi10Mg has a worse cavitation erosion resistance than the 3D printed one. This result is in accordance with the research of other authors [25] and seems very promising. Apparently, the study of cavitation erosion influence on 3D printed samples deserves an increased attention.

Better results of the 3D printed sample are probably related to the special structure produced by SLM method. As mentioned in [23], 3D printed AlSi10Mg samples possess a dendritic and fine structure. This kind of structure was also found in samples described in this thesis, see Fig. 66 (a).

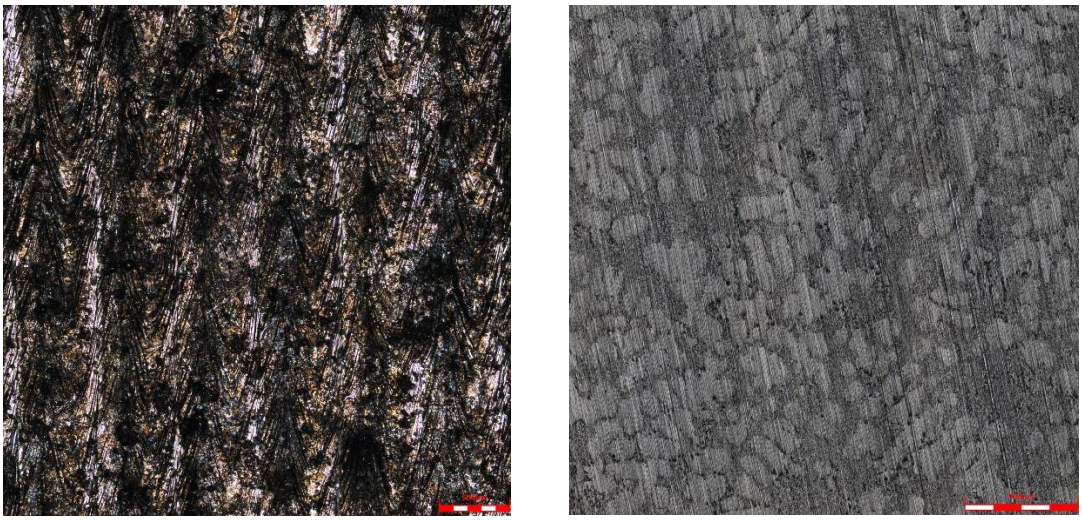

(a) (b)

Fig. 66: Comparison of 3D printed (a) and cast structure (b) of AlSi10Mg, *source: CEITEC*

According to [38], these samples exhibit the same or even better material characteristics in comparison to cast samples, including tensile strength, hardness and impact toughness. Based on the experiments performed in this thesis one can conclude that also cavitation erosion resistance can be added among these improved characteristics.

Conclusion and discussion

The thesis starts with a thorough literature search focusing on the cavitation principles, various mechanisms of cavitation erosion and a brief overview of laboratory methods of cavitation testing. The literature search provided a solid background for the experimental part and simultaneously showed that there are only very limited data concerning the investigation of the cavitation erosion resistance of 3D printed materials. For this reason, the goal of the experimental part was to examine (i) the resistance of selected 3D printed metal materials in comparison with the same materials prepared in a conventional way, (ii) to examine selected 3D printed plastic materials with respect to cavitation erosion and to perform their qualitative comparison.

Two kinds of tests were conducted – cavitation testing in a circuit with an orifice and a cavitating jet test. For every test the cavitation number was evaluated to assess the cavitation intensity.

In the former mentioned kind of test only the plastic samples were tested. However, no significant erosion was observed, even though the test lasted for 16 hours. This could be caused by quite high cavitation number (implying lower cavitation intensity). The only slightly apparent erosion was observed in PolyJet VeroClear, which might have been caused not only by the material characteristics, but also by the orientation of the ligaments, which were in this case oriented axially with respect to the tubular specimen. Other plastic materials were printed with their ligaments being oriented in a circumferential direction.

In the latter mentioned test, the cavitation erosion was much more apparent. In case of plastic materials, a dependence of cavitation erosion on compressive material characteristics was found. The material Antero 800NA with highest compressive yield strength (and/or compressive yield modulus, respectively) showed the lowest cavitation erosion. This observation could be beneficial in manufacturing of plastic armatures in hydraulic circuits or for small plastic pumps, respectively. Again, material PolyJet VeroClear showed the worst cavitation erosion resistance.

Metal specimens were manufactured by SLM method, which creates pores and molten pools in a structure of a material. However, the final structure shows good material characteristics.

In case of stainless steel 316L, it is very difficult to decide, which method of manufacturing is better, because the initial roughnesses of samples were significantly different. Nevertheless, it can be concluded that the samples prepared by the SLM method showed less percentual change of roughness and the surface even seemed to be smoother after the experiment. It is likely that the unmelted particles of the metal powder were released during the experiment. Moreover, a thin layer of oxides might have been created on the surface of the sample.

Specimen of 3D printed AlSi10Mg showed a better cavitation erosion resistance than the cast one. It is probably caused by the special structure produced by SLM, which improves material characteristics. This result suggests to consider the change in manufacturing of components made from this material.

In case of plastic materials, further examination is needed to determine the influence of orientation of ligaments. In addition, plastic materials should be also examined in a cavitating jet test with a lower input pressure in the nozzle (40 bar or 80 bar), because the cavitation intensity in this test was quite high, hence the obtained results might not be entirely reliable. On the other hand, in the circuit with the orifice the cavitation intensity was too low, thus no significant erosion was observed. Concerning the stainless steel 316L, more tests need to be conducted to make a proper conclusion which manufacturing method is more suitable with respect to the cavitation erosion resistance. In viewpoint of basic research, similar initial roughness of cast and 3D metal printed sample is essential to reach a decisive conclusion in this matter. However, it should be noted that one cannot expect that the roughness of components in real applications achieves the same value. More tests need to be conducted also in case of the aluminium alloy AlSi10Mg to examine the influence of heat and other finishing treatments of the SLM samples. Last but not least, the influence of various laser speeds of SLM also deserves to be studied.

References

[1] NOSKIEVIČ, Jaromír. *Kavitace v hydraulických strojích a zařízeních*. Praha: SNTL, 1989. ISBN 80-03-00206-0.

[2] KIM, Ki-Han, Georges CHAHINE, Jean-Pierre FRANC a Ayat KARIMI. *Advanced experimental and numerical techniques for cavitation erosion prediction*. Dordrecht: Springer, [2014]. Fluid mechanics and its applications, v. 106.

[3] JYOTI, K.K a A.B PANDIT. Water disinfection by acoustic and hydrodynamic cavitation. *Biochemical Engineering Journal*. 2001, **7**(3), 201-212. DOI: 10.1016/S1369-703X(00)00128-5. ISSN 1369703X. Also available at: http://linkinghub.elsevier.com/retrieve/pii/S1369703X00001285

[4] SUSLICK, Kenneth S., Millan M. MDLELENI a Jeffrey T. RIES. Chemistry Induced by Hydrodynamic Cavitation. *Journal of the American Chemical Society*. 1997, **119**(39), 9303-9304. DOI: 10.1021/ja972171i. ISSN 0002-7863. Also available at: http://pubs.acs.org/doi/abs/10.1021/ja972171i

[5] ROY, Samir Chandra. *Modeling and analysis of material behavior during cavitation erosion*. Cities of Grenoble, Saint-Martin-d'Hères & Gières, in France, 2015. Dissertation. Université Grenoble Alpes.

[6] BRENNEN, Christopher E. *Cavitation and bubble dynamics*. New York: Cambridge University Press, 2014. ISBN 978-1-107-64476-2.

[7] *Pulsed-laser-induced cavitation* [online]. 2010 [cit. 2018-11-22]. Available at: https://www.laserfocusworld.com/articles/2010/11/pulsed-laser-induced-cavitation-ultrafast-bubbles-enable-novel-nano-microfluidic-systems.html

[8] BRDIČKA, Miroslav, Ladislav SAMEK a Oldřich TARABA. *Kavitace: Diagnostika a technické využití*. Praha: SNTL, 1981.

[9] JÍZDNÝ, Martin. *Vlastní tvary vírového proudění* [online]. Brno, 2011. Also available at: https://www.vutbr.cz/www_base/zav_prace_soubor_verejne.php?file_id=3988. Diplomová práce. Vysoké učení technické v Brně, Fakulta strojního inženýrství.

[10] SUSLICK, K. S., Y. DIDENKO, M. M. FANG, T. HYEON, K. J. KOLBECK, W. B. MCNAMARA, M. M. MDLELENI a M. WONG. Acoustic cavitation and its chemical consequences. *Philosophical Transactions of the Royal Society A: Mathematical, Physical and Engineering Sciences*. 1999, **357**(1751), 335-353. DOI: 10.1098/rsta.1999.0330. ISSN 1364-503X. Also available at: http://rsta.royalsocietypublishing.org/cgi/doi/10.1098/rsta.1999.0330

[11] KINNAS, S. A. Theory and numerical methods for the hydrodynamic analysis of marine propulsors. *Unknown Journal*. 1996, (5), 279-322.

[12] SHIGLEY, Joseph Edward, Charles R MISCHKE a Richard G BUDYNAS, VLK, Miloš, ed. *Konstruování strojních součástí*. V Brně: VUTIUM, 2010. Překlady vysokoškolských učebnic. ISBN 978-80-214-2629-0.

[13] ŠOB, František. *Hydromechanika*. Vyd. 2. Brno: Akademické nakladatelství CERM, 2008. ISBN 978-80-214-3578-0.

[14] FRANC, Jean-Pierre a Jean-Marie MICHEL. *Fundamentals of cavitation*. Boston: Kluwer Academic Publishers, c2004. ISBN 14-020-2232-8.

[15] GONZÁLEZ-GARCÍA, José, Verónica SÁEZ, Ignacio TUDELA, María Isabel DÍEZ-GARCIA, María DESEADA ESCLAPEZ a Olivier LOUISNARD. Sonochemical Treatment of Water Polluted by Chlorinated Organocompounds. A Review. *Water*. 2010, **2**(1), 28-74. DOI: 10.3390/w2010028. ISSN 2073-4441. Also available at: http://www.mdpi.com/2073-4441/2/1/28

[16] Introduction to Cavitation. In: *The Process Piping* [online]. 2017 [cit. 2019-03-31]. Available at: https://www.theprocesspiping.com/introduction-to-cavitation/

[17] NIEVES-SOTO, Mario, Oscar M., Carlos ALBERTO, Marco ANTONIO, Toms VIVEROS-GARCA a Ignacio CONTRERAS-ANDRADE. Biodiesel Current Technology: Ultrasonic Process a Realistic Industrial Application. *Biodiesel - Feedstocks, Production and Applications*. InTech, 2012, 2012-12-03. DOI: 10.5772/52384. ISBN 978-953-51-0910-5. Also available at: http://www.intechopen.com/books/biodiesel-feedstocks-production-and-applications/biodiesel-current-technology-utrasonic-process-a-realistic-industrial-application

[18] REISMAN, G. E., E. A. MCKENNEY a C. E. BRENNEN. *Cloud cavitation on an oscillating hydrofoil* [online]. In: 1994, s. 2-3 [cit. 2019-02-08]. Available at: https://www.researchgate.net/publication/30760529_Cloud_cavitation_on_an_oscillating_hydrofoil

[19] Propeller Cavitation Explained. In: *The Shipyard* [online]. 2018 [cit. 2019-03-31]. Available at: https://www.theshipyardblog.com/single-post/2018/03/22/Propeller-Cavitation-Explained

[20] NOSKIEVIČ, Jaromír. *Kavitace*. Praha: Academia, 1969, 278 s. : il.

[21] ZHU, Y., J. ZOU, W. L. ZHAO, X. B. CHEN a H. Y. YANG. A study on surface topography in cavitation erosion tests of AlSi10Mg. *Tribology International*. 2016, **102**, 419-428. DOI: 10.1016/j.triboint.2016.06.007. ISSN 0301679X. Also available at: https://linkinghub.elsevier.com/retrieve/pii/S0301679X16301785

[22] KUIPER, G., Effects of artificial Roughness on Sheet Cavitation. *Inst. Of Mech. Eng.*,Second Conference on Cavitation,Edinburgh, 1983

[23] ZOU, J., Y. ZHU, M. PAN, T. XIE, X. CHEN a H. YANG. A study on cavitation erosion behavior of AlSi10Mg fabricated by selective laser melting (SLM). *Wear*. 2017, **376-377**, 496-506. DOI: 10.1016/j.wear.2016.11.031. ISSN 00431648. Also available at: https://linkinghub.elsevier.com/retrieve/pii/S0043164816308651

[24] THIJS, Lore, Karolien KEMPEN, Jean-Pierre KRUTH a Jan VAN HUMBEECK. Fine-structured aluminium products with controllable texture by selective laser melting of pre-alloyed AlSi10Mg powder. *Acta Materialia*. 2013, **61**(5), 1809-1819. DOI: 10.1016/j.actamat.2012.11.052. ISSN 13596454. Also available at: https://linkinghub.elsevier.com/retrieve/pii/S1359645412008592

[25] GIRELLI, Luca, Marialaura TOCCI, Lorenzo MONTESANO, Marcello GELFI a Annalisa POLA. Investigation of cavitation erosion resistance of AlSi10Mg alloy for additive manufacturing. *Wear*. 2018, **402-403**, 124-136. DOI: 10.1016/j.wear.2018.02.018. ISSN 00431648. Also available at: https://linkinghub.elsevier.com/retrieve/pii/S0043164817317805

[26] TANG, C. H, F. T CHENG a H. C MAN. Improvement in cavitation erosion resistance of a copper-based propeller alloy by laser surface melting. *Surface and Coatings Technology*. 2004, **182**(2-3), 300-307. DOI: 10.1016/j.surfcoat.2003.08.048. ISSN 02578972. Also available at: https://linkinghub.elsevier.com/retrieve/pii/S0257897203009460

[27] T6 Heat Treatment. In: *Action Sealtite* [online]. [cit. 2019-04-06]. Available at: https://www.actionsealtite.com/information-centre/t6-heat-treatment/t6-heat-treatment

[28] Hot Isostatic Pressing (HIP). In: *European Powder Metallurgy Association* [online]. [cit. 2019-04-06]. Available at: https://www.epma.com/hot-isostatic-pressing

[29] Introduction to FDM 3D printing. *3D HUBS* [online]. [cit. 2019-04-07]. Available at: https://www.3dhubs.com/knowledge-base/introduction-fdm-3d-printing

[30] What is PolyJet?. *GSC* [online]. 2017 [cit. 2019-04-07]. Available at: https://www.gsc-3d.com/articles/2017/11/what-polyjet-3d-printing-technology

[31] Metal 3D Printing Technology: Selective Laser Melting (SLM). *Sculpteo* [online]. [cit. 2019-04-07]. Available at: https://www.sculpteo.com/en/materials/slm-material/

[32] EOS Aluminium AlSi10Mg. In: *GPI Prototype* [online]. [cit. 2019-05-19]. Available at: https://gpiprototype.com/pdf/EOS_Aluminium_AlSi10Mg_en.pdf

[33] Safety data sheets. *Stratasys* [online]. [cit. 2019-05-19]. Available at: https://www.stratasys.com/sds

[34] Materiálové vlastnosti - Graf FDM. *MCAE Systems* [online]. [cit. 2019-04-26]. Available at: https://www.mcae.cz/wp-content/uploads/2018/01/Graf-FDM-CZ.pdf

[35] RUDOLF, Pavel, Martin JULIŠ, Lenka KLAKURKOVÁ, Pavel GEJDOŠ a Martin HUDEC. Cavitation erosion testing of different cavitation-resistent materials and coatings using the cavitating jet method. *IOP Conference Series: Earth and Environmental Science*. 2019, **240**. DOI: 10.1088/1755-1315/240/6/062057. ISSN 1755-1315. Also available at: http://stacks.iop.org/1755-1315/240/i=6/a=062057?key=crossref.ce3f56dec26dab1c215bd139bb6aa70e

[36] ARNDT, Roger Edward Anthony, Gary John BALAS a Martin WOSNIK. Control of Cavitating Flows: A Perspective. JSME International Journal Series B. 2005, **48**(2), 334-341. DOI: 10.1299/jsmeb.48.334. ISSN 1340-8054. Also available at: http://joi.jlc.jst.go.jp/JST.JSTAGE/jsmeb/48.334?from=CrossRef

[37] BRENNEN, Christopher E. (2007) *The Amazing World of Bubbles.* Engineering and Science, 70 (1). pp. 30-41. ISSN 0013-7812; http://resolver.caltech.edu/CaltechES:70.1.Bubbles

[38] KEMPEN, Karolien, Lore THIJS, Jan VAN HUMBEECK a Jean-Pierre KRUTH. Mechanical properties of AlSi10Mg produced by Selective Laser Melting. *Physics Procedia* [online]. 2012 [cit. 2019-05-19]. ISSN 1875-3892.

[39] Magneticko indukční průtokoměry. *ELA - měřidla pro vodárenství* [online]. [cit. 2019-05-20]. Available at: http://www.elabrno.cz/cs/magneticko-indukcni-prutokomery-mqi-si/

[40] DMP 331: stainless steel sensor. *BD SENSORS* [online]. [cit. 2019-05-20]. Available at: http://www.bdsensors.cz/fileadmin/user_upload/Download/Datenblaetter_datasheets/DMP331_CS.pdf

[41] Nozzles & washing accessories. *R-M Nederland* [online]. [cit. 2019-05-20]. Available at: https://r-mnederland.nl/product-category/nozzles-washing-accessories/

Symbols and abbreviations

Roman letters

Symbol	Unit	Explanation
du/dx	s^{-1}	Velocity gradient
A_0	m	Initial radius of the cloud of bubbles
c	$m \cdot s^{-1}$	Speed of sound
C_p	-	Pressure coefficient
C_{pmin}	-	Minimum of the pressure coefficient
d	m	Diameter of the micro jet
D	μm	Pit diameter
D_H	m	Characteristic dimension (in Reynolds equation)
h	μm	Pit depth
k	$kg\ m^{-n} \cdot s^{n-1}$	A proportionality coefficient in Eq. (3.5)
l	m	Linear dimension of the plasticized area
$\dot{m}$	$kg \cdot s^{-1}$	Mass loss
n	-	Exponent in Eq. (3.5)
p_B	Pa	Homogenous (uniform) pressure in the bubble
p_{cav}	Pa	Cavitation pressure
p_k	Pa	Pressure of the surrounding liquid
p_φ	Pa	Velocity of a vortex in its core
p_v	Pa	Saturated vapor pressure
p_∞	Pa	Pressure at an infinite distance from the bubble (reference pressure)
$p(r,t)$	Pa	Pressure field
$p(x_i)$	Pa	Pressure
r	m	Radial coordinate
r_φ	m	Radius of a vortex
R	m	Bubble radius
R_0	m	Initial bubble radius
$\dot{R}$	$m \cdot s^{-1}$	Velocity of a bubble wall motion
$\ddot{R}$	$m \cdot s^{-2}$	Acceleration of a bubble wall motion
Re	-	Reynolds number
$u(r,t)$	$m \cdot s^{-1}$	Outward velocity
v	$m \cdot s^{-1}$	Flow velocity
v_0	$m \cdot s^{-1}$	Ultimate flow velocity at which cavitation still occurs
v_φ	$m \cdot s^{-1}$	Circumferential velocity of the potential vortex
$v_i(x_i)$	$m \cdot s^{-1}$	Velocity field
v_j	$m \cdot s^{-1}$	Velocity of the jet
V^*	mm^3	Characteristic erosion volume loss

Greek letters

Symbol	Unit	Explanation
α_0	-	The volume fraction of the gas enclosed in the cloud of bubbles
β	-	Parameter for description of the cloud of bubbles
$\Delta\varepsilon$	-	Relative elongation caused by shock stress
Δp	Pa	Pressure generated by micro jet
Δt	s	Duration of the pressure pulse
$\dot{\varepsilon}$	s^{-1}	Strain rate
ε_{max}	-	Maximum strain
θ	-	Material characteristics in Eq. (3.7)
μ	Pa·s	Dynamic viscosity of a liquid
ν_L	$m^2 \cdot s^{-1}$	Kinematic viscosity of a liquid
ρ	$kg \cdot m^{-3}$	Liquid density
σ	-	Cavitation number
σ_i	-	Critical cavitation number
σ_L	$N \cdot m^{-1}$	Surface tension at an liquid/bubble interface
τ	Pa	Shear stress
ω	$rad \cdot s^{-1}$	Turbulence

Abbreviations

FDM	Fused Deposition Modeling
SLM	Selective Laser Melting
DMLS	Direct Metal Laser Sintering